Engineered Infected Epidermis Model for *In Vitro* Study of the Skin Proinflammatory Response

by

Maryam Jahanshahi
Bachelor of Applied Science, Sharif University of Technology, 2016

A Thesis Submitted in Partial Fulfillment
of the Requirements for the Degree of

MASTER OF APPLIED SCIENCE

in the Department of Mechanical Engineering

# Supervisory Committee

Engineered Infected Epidermis Model for In Vitro Study of the Skin Proinflammatory Response

by

Maryam Jahanshahi
Bachelor of Applied Science, Sharif University of Technology, 2016

**Supervisory Committee**

Dr. Mohsen Akbari, Department of Mechanical Engineering
**Supervisor**

Dr. Rodney Herring, Department of Mechanical Engineering
**Departmental Member**

# Abstract

**Supervisory Committee**
Dr. Mohsen Akbari, Department of Mechanical Engineering
**Supervisor**
Dr. Rodney Herring, Department of Mechanical Engineering
**Departmental Member**

Wound infection is a major clinical burden that can significantly impede the healing process and cause severe pain. Prolonged wound infection can lead to long-term hospitalization or death. Pre-clinical research to evaluate new drugs or treatment strategies relies on animal studies. However, animal studies have several challenges including interspecies variations, cost, and, ethics question the success of these models. Recent advances in tissue engineering have enabled the development of in vitro human skin models for wound infection modeling and drug testing. The existing skin models are mostly representative of the healthy human skin and its normal functions. However, to study the wound healing process and the response of skin to the infection, there is still a need to develop a skin model mimicking the wound infection. This work presents a simplified functional infected epidermis model, fabricated with enzymatically crosslinked gelatin hydrogel. The immortalized human keratinocytes, HaCaT cells, was successfully cultured and differentiated to a multilayer epidermis structure at the air-liquid interface, and expressed terminal differentiation marker, filaggrin, in the outer layer. The barrier function of the epidermis model was studied by measuring the electrical resistance and tissue permeability across the layer. The results showed that the developed epidermis model offered a higher electrical resistance and a lower drug permeability compared to the cell monolayer on gelatin and cell-free gelatin. To show the capability of the developed epidermis model in wound modeling and drug, the model was infected with *Escherichia*

*coli* and the inflammatory response of keratinocytes was studied by measuring the level of proinflammatory cytokines, including IL-1β and TNF-α. The results demonstrated the proinflammatory response of the epidermis model to infection by producing a higher level of TNF-α and IL-1β compared to the control group. While treating with antibiotic ciprofloxacin terminated the proinflammatory response and reduced the level of TNF-α and IL-1β. The robust fabrication procedure and functionality of this model suggest that this model has great potential for wound modeling and high throughput drug testing.

# Table of Contents

# List of Tables

# List of Figures

# List of Abbreviations

PDGF - platelet-derived growth factor

TGF-A1 - transforming growth factors A1

TGF-2 - transforming growth factors 2

ROS - reactive oxygen species

ECM - extracellular matrix

VEGF - vascular endothelial growth factor

FGF-2 - fibroblast growth factor 2

MMPs - matrix metalloproteinase enzymes

CD31 - cluster of differentiation 31

HUVECs - human umbilical vein endothelial cells

RGD - Arg-Gly-Asp

UV – ultraviolet

mTG - microbial transglutaminase

DPBS - Dulbecco's phosphate-buffered saline

HaCaT - immortalized human keratinocyte

SEM - scanning electron microscopy

DMEM - Dulbecco’s Modified Eagle Media

MEMS - micro-electromechanical system

PDMS – Polydimethylsiloxane

OCT - optimal cutting temperature

TLRs - Toll-like receptors

PRRs - pattern recognition receptors

PAMPs - pathogen-associated molecular patterns

NF-κB - nuclear factor-κB

LPS – liposaccharide

E. coli - Escherichia coli

TNF-α - tumor necrosis factor alpha

IL-1β - interleukin 1 beta

LB – liquid broth

CFU - colony forming unit

qPCR - quantitative polymerase chain reaction

# Acknowledgments

I would like to thank my supervisor, Dr. Mohsen Akbari, for his great support and guidance during my graduate study. Without his useful and constructive feedback this work would never be completed successfully. His patience, encouragement, and enthusiasm were always inspiring for me.

I would like to express my sincere appreciation to Dr. Patrick Walter for his kind advisory and answering my biology questions throughout my research.

I would like to thank Dr. Rodney Herring for his helpful lectures in microscopy techniques which significantly improved my imaging skills for this project.

I also would like to thank my fellow lab members especially Brent Godau, Ehsan Samiei, and David Hamdi for teaching me their skills in research and helping me in experiments.

Last but not least, I would like to express my deep gratitude to my parents, sisters, and boyfriend for their unconditional love, support and continuous encouragement throughout my study, research and writing this thesis.

# Dedication

This thesis is dedicated to my family for their endless love and support.

# Chapter 1: Introduction

## 1.1. Skin anatomy

Skin is the outermost and largest human organ. The multilayer structure of the skin consists of epidermis, dermis, and hypodermis layers as well as hair follicles, blood vessels, sweat glands, and sebaceous glands (Figure 1) [1]–[5]. This complex structure accounts for the skin's vital functions in regulating body temperature, sensation, and protection of the human body against mechanical, chemical, and biological insults [1], [2], [5], [6].

The epidermis has a varying thickness from 0.1 mm up to 1.5 mm depending on the body site. It is composed of multiple layers of keratinocytes with different degrees of differentiation which are arranged into four regions; stratum corneum, stratum granulosum, stratum spinosum, and stratum basale (Figure 1) [2], [5]. Stratum corneum is the unique feature of the epidermis layer in which terminally differentiated keratinocytes (coenocytes) are embedded in the intercellular lipid matrix. This "bricks and mortar" structure makes the epidermis as an effective barrier to water loss and environmental pathogens [1], [6]. The next inner layer of the epidermis, stratum granulosum, consists of non-dividing keratinocytes while the following layer, stratum spinosum, is composed of keratinocytes with limited division capacity. The basale layer is where keratinocytes divide and undergo a series of cellular differentiation processes while moving upward to the stratum corneum [1], [2], [5]. In addition to keratinocytes, other cell types such as melanocytes, Langerhans and Merkel cells are present in the epidermis layer [1], [3]–[5]. Beneath the epidermis, the collagen-rich dermis layer is responsible for providing mechanical support and withstanding applied external forces. Other than collagen, elastin fibers in the dermis play

a critical role in providing elastic properties of skin [3]–[6]. The main cell type of the dermis is fibroblast but several types of innate immune cells such as macrophages, mast cells, and innate lymphoid cells are found in this layer [6]. In contrast to the avascular structure of the epidermis, the dermis layer contains blood vessels for nutrient delivery and waste transport (Figure 1). Additionally, other components including sweat glands, hair follicles, sebaceous glands, and nerves present in the dermis [1], [3], [4]. The lowermost layer is hypodermis. The main resident cells of the hypodermis region are fibroblasts, adipocytes, and macrophages. The hypodermis functions as thermal insulation, shock-absorber, and energy supply [1], [4].

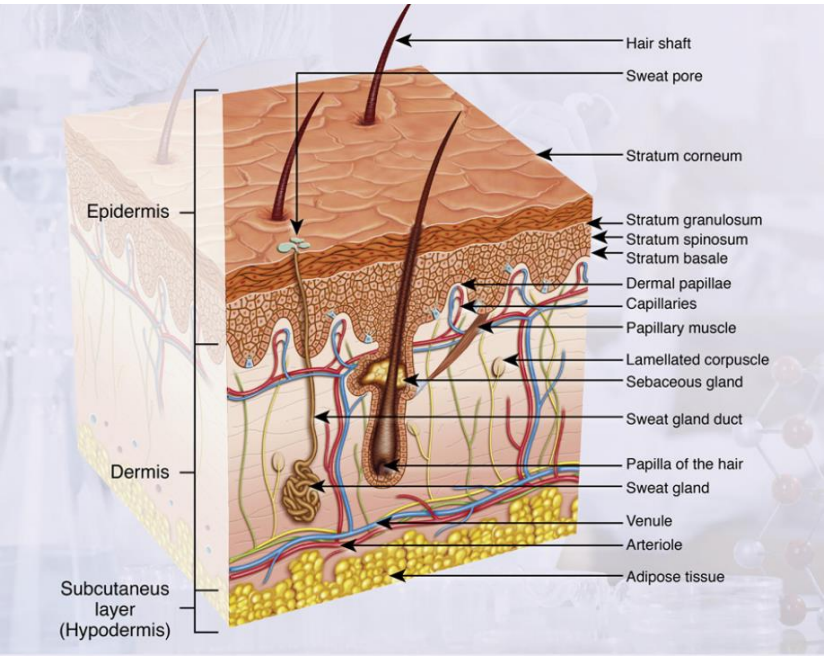


**Figure 1. Schematic picture of the native skin representing its three main layers; epidermis, dermis, and hypodermis and skin appendices including hair follicles, sebaceous glands and blood vessels** [4]**.**

## 1.2. Skin Wounds

Skin wounds are the fourth prevalent skin problem in the United States. A large number of people are affected by either infected or chronic wounds worldwide and a considerable share of the annual health cost is dedicated to treating them [7]. In the United States alone, in 2009, over 6.5 million patients suffered from skin wounds and their treatments cost over US$ 25 billion annually [8]. Skin wounds can be categorized into two major groups; acute wounds and chronic wounds. The healing process of acute wounds is well-organized and predictable in which platelets, keratinocytes, fibroblasts, vascular cells, and immune cells repair the skin tissue and restore its integrity [9], [10]. In contrast to acute wounds that usually heal without major interventions, in chronic wounds, the normal healing process is disabled by cellular and molecular abnormalities [9].

### 1.2.1. Acute Wounds and Normal Wound Healing

The normal wound healing process includes 4 phases; coagulation, inflammation, proliferation (formation of granulation tissue), and remodeling (maturation and scar formation) (Figure 2). The coagulation phase is initiated immediately after the injury by platelets adhering to the damaged blood vessels (Figure 2 A) [9]. Multiple growth factors, cytokines, and other survival or apoptosis-inducing factors are released by platelets at the injury site. Among these factors, platelet-derived growth factor (PDGF) and transforming growth factors A1 and 2 (TGF-A1 and TGF-2) play pivotal roles in initiating the inflammatory phase by attracting leukocytes, neutrophils, and macrophages. Leukocytes clear foreign bodies and bacteria from the wound area by releasing reactive oxygen species (ROS) and proteases [9], [10].

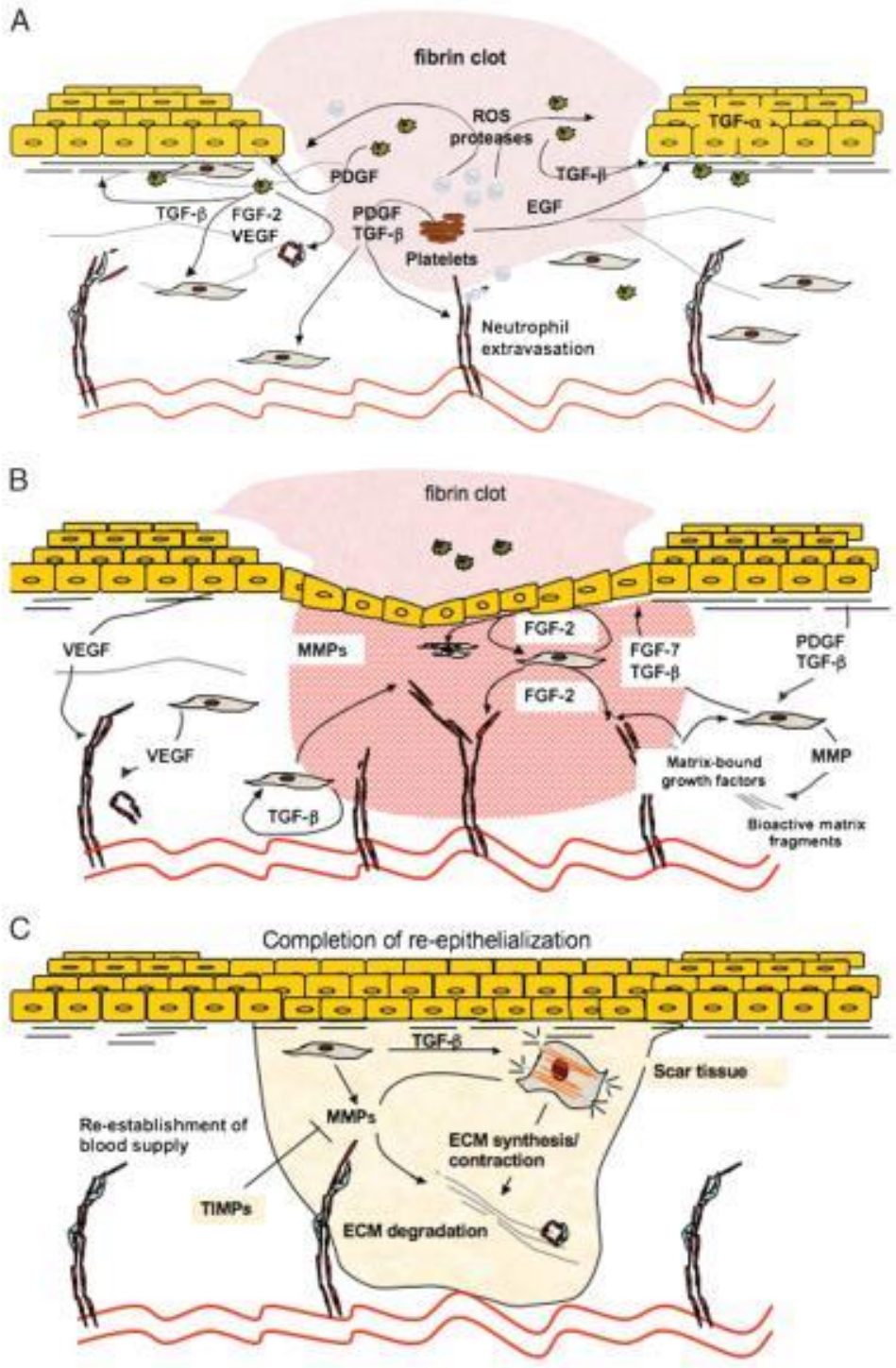


**Figure 2. Mechanism of normal wound healing. Normal wound healing processes can be divided into 4 overlapping phases: coagulation (not shown), A) inflammatory phase, B) proliferative phase/granulation tissue formation, and C) remodeling phase** [9]**.**

The resolution of inflammation occurs within a few days post-injury with the help of anti-inflammatory cytokines and bioactive lipids [9], [10]. Subsequently, when the haemostasis has been achieved, the proliferation phase begins by dermal and epidermal cells migration and secretion of extracellular matrix (ECM) (Figure 2 A, B) [10]. This event is accompanied by wound healing angiogenesis to supply substantial nutrients and facilitate the gas and metabolite exchange within the wound bed [9]. The angiogenesis is induced by the release of vascular endothelial growth factor (VEGF), fibroblast growth factor 2 (FGF-2), and PDGF by platelets and resident cells at the wound site. These factors trigger the migration of endothelial cells to the wound site from new blood vessels [9], [10].

As a desirable microenvironment for the proliferation of epidermal and dermal cells has been provided, the final phase of healing begins. In the remodeling phase, fibroblasts proliferate and deposit ECM which results in the formation of granulation tissue within the wound. This event is accompanied by ECM maturation in which collagen I bundles diameter increase to be substituted for collagen III, fibrin, fibronectin, and hyaluronic acid (Figure 2 C). In this phase, matrix-remodeling enzymes such as matrix metalloproteinase enzymes (MMPs) are pivotal in degrading collagen and remodeling the local matrix to facilitate cell migration, proliferation and angiogenesis processes. Finally, acellular scar tissue forms by apoptosis of fibroblastic cells [9]. This phase may last for 1 year or a longer period [10].

### 1.2.2. Chronic Wounds

Minor injuries such as insect bites or even simple scratches of dry skin which would heal within a few days in healthy individuals can turn to a nonhealing chronic wound in patients

with diabetes or obesity (Figure 3). Infection and drug-resistant microbial biofilms significantly contribute to the chronicity of wounds and mortality [9], [10].

**Figure 3. Examples of chronic wound**s [11]**.**

The burden of treating chronic wounds and health care costs drastically increases by growing the number of patients suffering from diabetes and obesity worldwide [8]. Chronic wounds can be categorized into 4 major groups; venous ulcers, arterial ulcers, pressure ulcers, and diabetic ulcers (Table 1) [8], [9]. Although the underlying pathologies of these wounds are different, there are several common features between them such as long-lasting inflammatory phase, persistent infection, drug-resistant microbial biofilms formation, and lack of dermal and epidermal cells ability to respond properly [9]. Accumulation of excessive inflammatory cells at chronic wound sites results in the synthesis of different ROS which damages the ECM and cell membrane and eventually causes premature cell senescence. Moreover, the ROS and proinflammatory cytokines increase the production of serine proteinases and MMPs. These enzymes can degrade the ECM and decrease the bioavailability of growth factors which are critical for normal cell function in the healing process [9].

**Table 1. Major types of chronic wounds** [9]

| Wound Type | Pathology | No. of Affected Patients | Cost of Treatment | Total Annual Cost |
|---|---|---|---|---|
| **Venous ulcers** | Venous insufficiency, thrombosis, varicosis | 400,000–600,000 | $5000–$10,000 | $1.9 billion to $2.5 billion |
| **Arterial ulcers** | Macroangiopathy, atherosclerosis, arterial insufficiency | 100,000 | $9000–$16,000 | Arterial ulcers |
| **Diabetic ulcers** | Neuropathy, microangiopathy, hyperglycemia | 2 million | $6000/patient | $150 million |
| **Pressure ulcers** | Immobility, excessive pressure | 1.3 million to 3 million | Up to $70,000 | $3.5 billion to $7.0 billion annually |

Venous ulcers account for over 70% of ulcers in the lower leg [8]. Venous ulcers indicate significant pathological changes in the deep and superficial veins which result in a constant blood backflow and increasing venous pressure. The resulting pressure causes the leakage of fibrin and other plasma components to the surrounding area. Increasing the level of fibrin at the wound site down-regulates the production of collagen as well as forming pericapillary fibrin cuffs which interfere with the normal functions of vessels. These events result in blockage of blood-derived growth factors and failure of the normal wound healing process [9].

Arterial ulcers can be the result of arterial lumen narrowing and ischemia by atherosclerosis or embolism. In contrast to venous ulcers, arterial ulcers are less prevalent and can be present in other locations on the body, rather than between the ankle and the knee, for example a toe [9].

Pressure ulcers are more common among the elderly, stroke patients, diabetic patients, and people with limited mobility and impaired sensation [8]. Pressure ulcers can be

developed under long-lasting pressure and shear forces which result in oxygen tension reduction and tissue necrosis [9].

Diabetic ulcers can be the result of neuropathy, muscle metabolism deficiencies, and several microvascular complications due to hyperglycemia. Diabetic neuropathy is a type of foot's nerve damage and can lead to foot deformities and ulcers. It has been estimated that about 25% of patients with diabetes will suffer from diabetic ulcers. Diabetes also can cause or worsen arterial, venous, and pressure ulcers [9]. Diabetic patients have less deformable red blood cells with higher viscosity which causes vascular stasis in microcirculation. Moreover, the high glycosylated hemoglobin affinity for oxygen interferes with the oxygen delivery to ischemic tissues. Diabetic ulcers usually display a lower level of the inflammatory response, fibroblast proliferation and collagen deposition which lead to tensile strength decrease. Additionally, the decreased ability of macrophages in bacteria digestion exacerbates the infection at the wound site and makes the treatment more challenging [11].

In all types of chronic wounds, infection as an external factor can interfere with the healing process and cause mortality in some cases [12]. Both live bacteria and bacterial toxins lead to the recruitment of excessive inflammatory cells. The expressed proteases including MMPs by inflammatory cells and bacteria degrade the ECM and necessary growth factors at the wound site [13]. Additionally, bacteria colonization at the wound site can make biofilms which are favorable microenvironments for bacteria survival. The surrounded bacteria by secreted polymer matrix are safe from host immune defense and antimicrobial agents [14]. Although the adverse effect of biofilms on the wound healing process is well-established, the precise mechanism of this interference is still unclear. In

addition to the higher survival rate of bacteria and increasing production of toxins, there can be other possible explanations including the presence of toxic components in the polymer matrix which can impede the host cells' functions. A better understanding of these mechanisms is helpful in optimizing approaches for biofilm prevention or elimination [9].

The huge impact of wounds on the quality of human life and the increasing cost of wound treatments necessitate more comprehensive studies to understand wound healing mechanisms [8]. Chronic wounds can be treated if the impediments to wound healing are identified and managed [11]. The existing approaches based on the current understanding of the biological mechanism of wound healing need to be improved and personalized in some cases to produce better therapeutic outcomes [9]. In addition to understanding the wound healing mechanism, optimizing therapeutic and regenerative agents is a necessary step to prevent or overcome the chronicity [8], [11]. Currently, there is no hard evidence to prove the superiority of one therapeutic agent to any other and most of these compounds fail in topical administration due to the poor penetration capacity or presence of biofilms [1], [9]. Therefore, it is required to design and optimize more efficient drug delivery systems as well as enhancing therapeutic molecules to successfully eliminate drug resistant biofilms and accelerate the tissue repair process [1], [9]. The conventional topical drug administration approaches include using liquids (e.g. sprays), semisolids (e.g. ointments), and solids (e.g. patches). However, the emergence of smart drug delivery systems such as nanoparticles, microneedles, and vesicular carriers has opened a new avenue to overcome the skin barrier and minimize the undesirable drug side-effects (Figure 4) [1]. Studying the wound healing mechanism and preclinical testing of new therapeutics as well as optimizing

novel drug delivery systems call for the allocation of a large number of well-defined skin models to achieve more reliable results [1], [4], [15], [16].

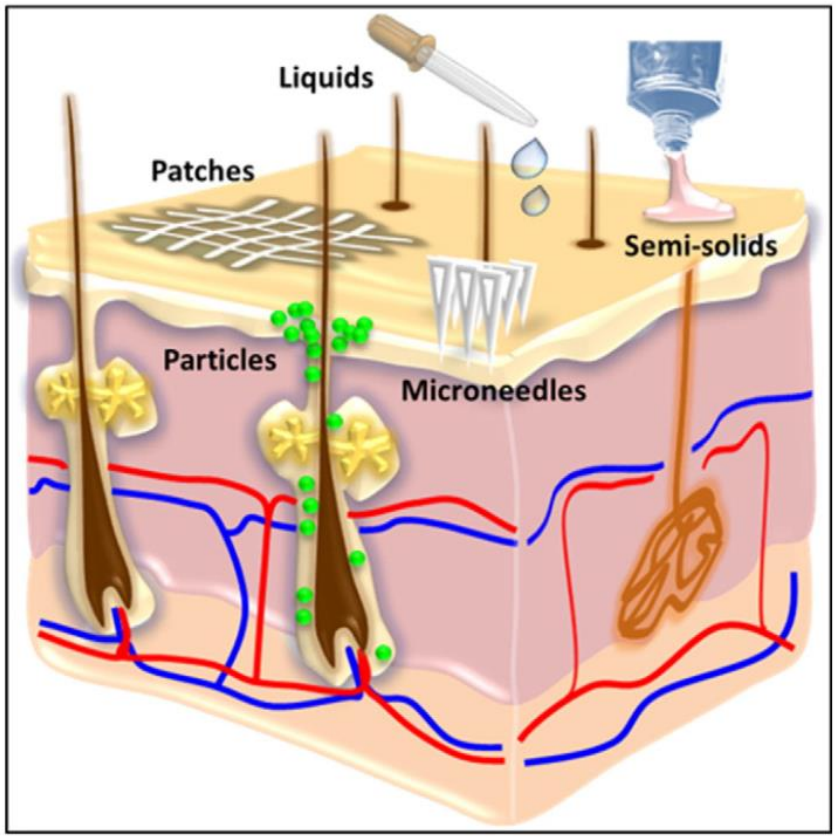


**Figure 4. Established and novel drug delivery systems for topical drug application** [1].

## 1.3. Skin Models

Current high throughput drug development research and studying the efficacy of drug delivery systems mainly relies on animal [17]–[22], *ex vivo* [23]–[29], and *in vitro* models [30]–[42]. Depending on the stage of studies each group can be helpful in evaluating therapeutic agents or drug delivery systems [43].

### 1.3.1. Animal Models

The rate of using animal models for studying novel therapeutics and drug delivery systems has been increasing [44]. The key concept of using animal models is an analogy between the target phenomenon required to be studied and the animal that is being investigated instead. The significance and validity of the data obtained from animal studies and translated with respect to human physiology depend on the selection of an appropriate animal model [45]. Small animals such as mice, rats, and rabbits are more common for studies with a large number of experiments and samples. However, the wound healing mechanism in rodents mainly relies on wound contraction (Figure 5 A) and differ from the migration of epidermal cells in human. This difference can account for 53% similarity of results between small animals and human, while this number increases to 78% between pig and human due to their similarities in dermal architecture, skin thickness, follicular structure, and abundance of subdermal adipose tissue (Figure 5 B) [44], [46]. Nevertheless, the results obtained from studies on small animals are still valuable in the early stages of studying wounds, infection, and host-pathogen interaction [18]–[22], [47]–[50].

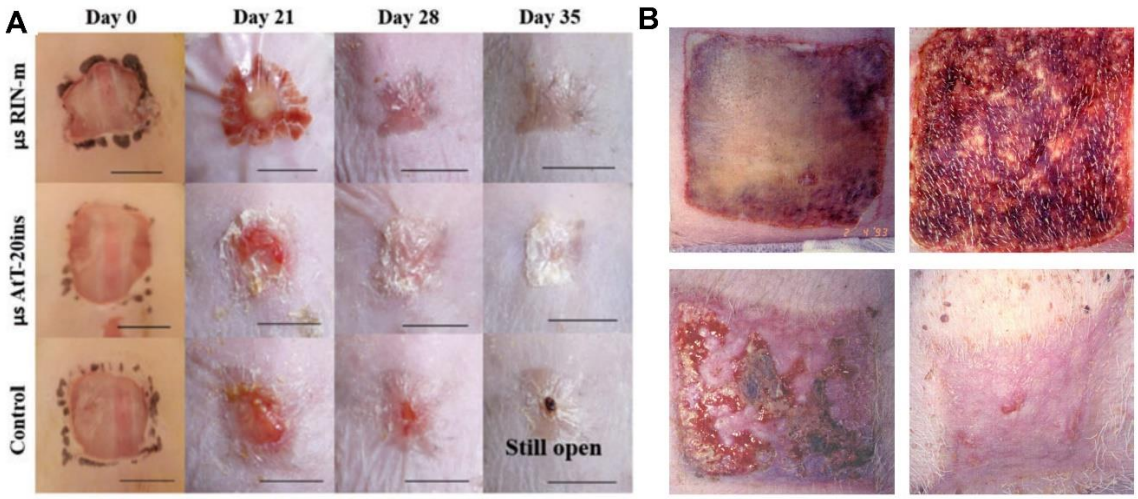


**Figure 5. Animal wound models. A) representative images of wound closure on mouse model** [18]**, B) representative images of wound healing on pig model in response to Silversulphadiazine cream treatments** [46]**.**

Even considering that human drug development owes to preclinical animal studies, it cannot turn its drawbacks negligible. In 2009, Niall Shanks *et al* challenged the idea that animal models can be predictive for humans [51]. In 2019, in a thorough study by Jarrod Bailey and Michael Balls, it was observed that a new drug with a 70% chance of being nontoxic in humans from *in vitro* data, displayed an average of 74% of being nontoxic on five different animals. It demonstrates that animal studies do not necessarily provide additional validity in clinical results [52]. Moreover, according to Human Society International, 9 out of 10 drugs with safe and effective results in animal studies fail in clinical trials [53]. Other than the reliability of the results from animal studies, the high cost (>$800 million per drug) and ethical issues of using animals in research studies give a arise to a major conflict. According to a study by Bhanu Prasad CH, every year over 26 million animals in the United States anole are used for scientific and commercial studies

[54]. The above-mentioned challenges with animal studies brought researchers' attention to the other alternative models.

### 1.3.2. *Ex Vivo* Models

*Ex vivo* human skin obtained from surgical procedures (Figure 6) has been used for years as a model to study skin wounds [23], [55], testing drug permeation [28], [29], and skin infection [15], [26], [27]. In 2017, Christoph Schaudinn *et al* used human skin explants for chronic wound modeling and studying the host-pathogen interactions and efficacy of antimicrobial agents. It is claimed that one of the major advantages of *ex vivo* wound models is the quantifiable bacterial infection, measurable donor-dependent immune response, and good repeatability of the results [23]. In 2019, Daniel J. Yoon *et al* showed the results of their studies on an *ex vivo* infected wound model and noted that the absence of a systemic inflammatory response and cellular recruitment may limit the model's applications but still it would still be a good asset for studying the local innate immune response of skin to injury and infection [55].

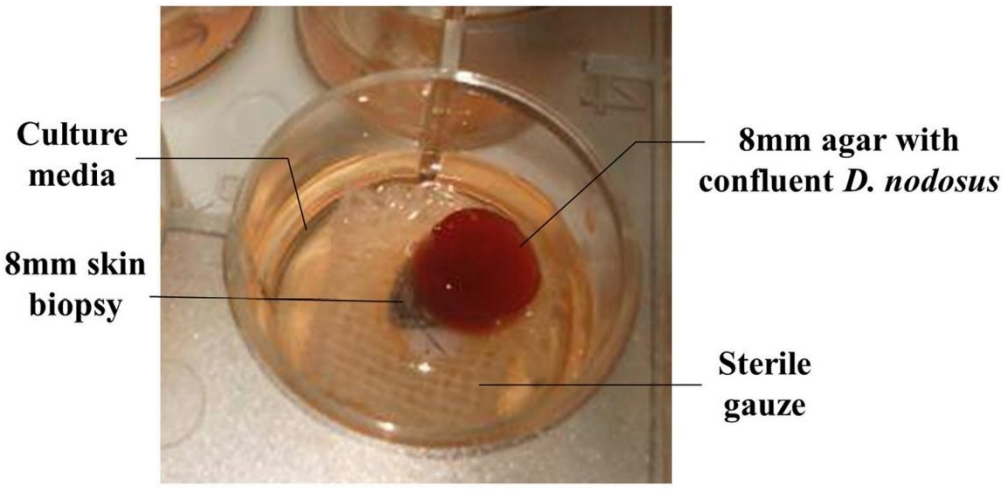


**Figure 6. Assembled 3D skin explant model for anaerobic bacterial infection** [24]**.**

However, difficulty finding donors, the short life span of excised tissues, and the metabolism and biotransformation of chemicals applied to the skin after excision of the tissue from the donor hinder the use of *ex vivo* models for high throughput studies [1], [4], [16]. Such issues led to the widespread use of *in vitro* models [1].

### 1.3.3. *In vitro* Models

*In vitro* models emerged initially as two-dimensional (2D) cell culture and evolved to three-dimensional (3D) models [34], [43], [56]. 2D cell culture is a monolayer of cells cultured on solid flat surfaces such as plastic multi-well plates. The cells are in a fluid medium which supplies nutrient, growth factors, and required gases [57]. 2D monolayers of dermal keratinocytes and fibroblasts are widely used for different studies such as studying the skin inflammatory response [30], [31], [35]–[37], [58] and drug cytotoxicity tests [38], [39]. Although this low-cost method is helpful in quickly identifying toxic compounds at the very early research stages [1], [43], [57], [59], the obtained results are not necessarily translatable to the 3D microenvironment of the native tissue [1], [56], [57]. This discrepancy can be due to the lack of sufficient cell-cell and cell-matrix interactions which are essential for normal physiological and pathological processes involved in cell responses to events in the environment such as injury or toxic compounds [1], [57], [60]. Tau Sun *et al*, in 2006, studied the cytotoxic effect of hydrogen peroxide on endothelial, human dermal fibroblasts, and human keratinocytes viability in 2D and 3D cultures. Their results showed that as the concentration of hydrogen peroxide increased, the cell viability decreased in both 2D and 3D cultures of all cell types. However, this effect was more significant on 2D cell culture which demonstrates that cells in 3D culture are more resistant to hydrogen peroxide at different concentrations (Figure 7) [59]. In addition, the

application of 2D monolayers is limited to studying the target compound in liquid. For semi-solid and solid target compounds, indirect methods of study are required. A further limitation, the 2D culture of keratinocytes is not able to form a mature epidermal tissue functioning as a barrier for drug permeation studies [1].

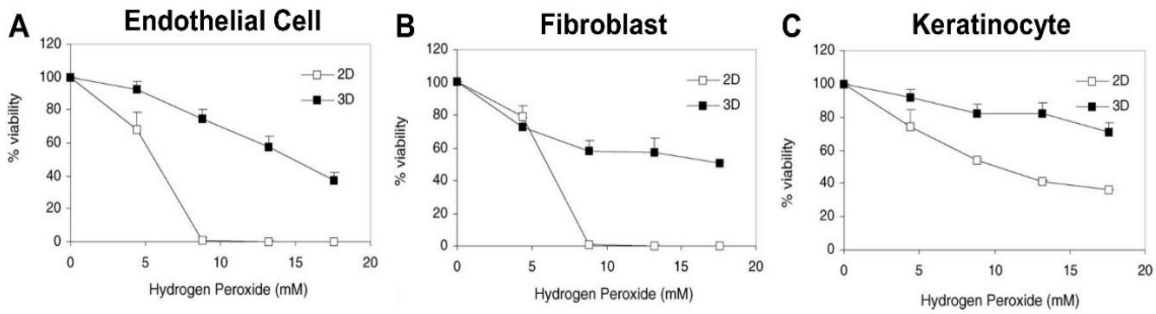


**Figure 7. Effects of hydrogen peroxide on cell viability of A) endothelial cells, B) human dermal fibroblasts, and C) human keratinocytes in 2D and 3D cultures** [59].

As an alternative to the animal, *ex vivo*, and 2D models, recently in the past two decades, there has been a tendency towards the development of engineered *in vitro* 3D models. 3D models started from multilayered sheets of keratinocytes [40], [41] and evolved to reconstructed full-thickness human skin models using cell inserts [32]–[34], [42], microfluidics [53], [61], [62], and 3D printing [63]–[65]. Multilayered sheets of human keratinocytes known as reconstructed human epidermis model isare obtainable by differentiating keratinocytes at air-liquid-interface after reaching a confluent monolayer in submerged culture (Figure 8) [1], [40], [41]. Reconstructed human epidermis models can be used in different studies including bacterial colonization, drug testing, and skin proinflammatory response [1], [41]. Coculturing dermal fibroblasts with keratinocytes serving as a dermis layer enhances the cell signaling and improveimproves the cell -specific

responses [1]. Geuranne Tjabringa *et al*, in 2008, developed a human skin model consisting of epidermis and dermis layers to study psoriasis which is an inflammatory skin disease driven by aberrant interactions between the epithelium and the immune system. Their results showed the potential of this disease model to the *in vitro* study of the molecular pathology and pharmacological intervention [66].

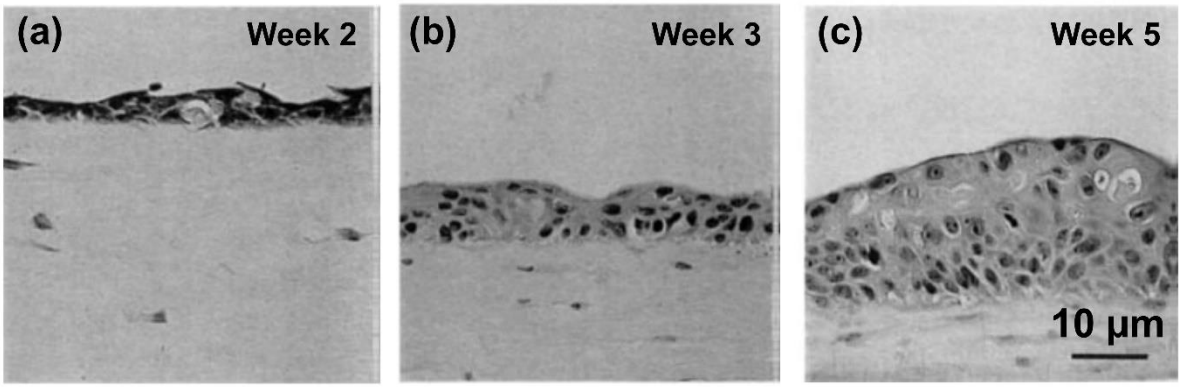


**Figure 8. Histologic appearance of HaCaT cells cultured at air-liquid-interface** [40]**.**

More complex structures representing human skin equivalent usually include more details such as, hypodermis layer [33], [63], vascularization [53], [63], [64], [67], [68] or neural cells [33]. There are different methods to create a vasculature channel. Maierdanjiang Wufuer *et al* used microfluidics technology to form the endothelium (Figure 9 A) [53] while Nobuhito Mori *et al* successfully created a perfusable vascular channel by embedding nylon wires into the collagen hydrogel and removing them after crosslinking collagen to make a hollow network channel (Figure 9 B) [67].

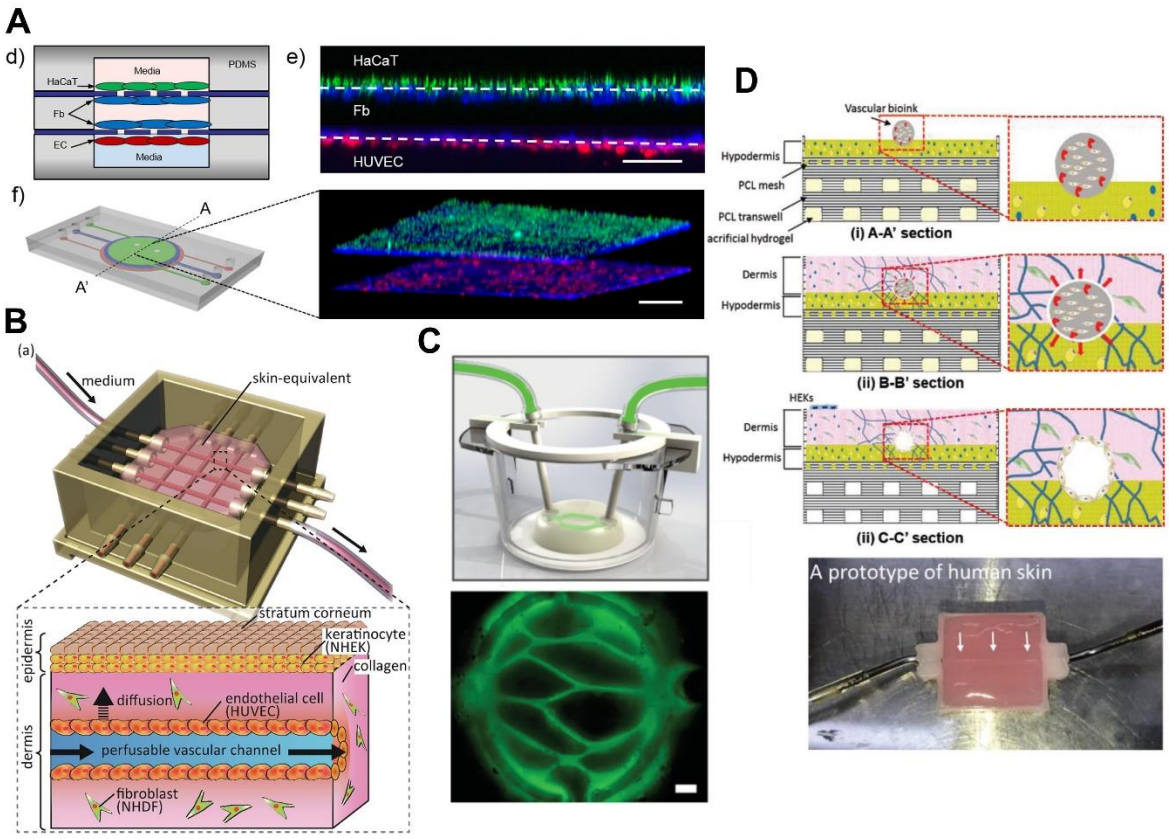


**Figure 9. Representative of techniques used in developing vascularized skin models. A) using microfluidic devices** [53]**, B) using nylon threads** [67]**, C) using 3D printed sacrificial materials** [64]**, and D) using 3D printed cell-incorporated hydrogels** [63]**.**

3D printing has been playing a critical role in taking the reconstructed human skin models to an advanced level. Hasan E. Abaci *et al* applied 3D printing to make a microchannel mold and filled it with sacrificial alginate (Figure 9 C). After casting the dermal compartment consisting of dermal fibroblasts and collagen, the sacrificial alginate was removed by sodium citrate treatment. They confirmed the formation of lumens by iPSC-derived endothelial cells with immunofluorescent staining of the cluster of differentiation 31 (CD31) expressed by endothelial cells [64]. In 2018, Byoung Soo Kim *et al* utilized a 3D bioprinting method to fabricate a novel full-thickness skin model

consisting of epidermis, dermis, hypodermis, and vasculature (Figure 9 D). The vascular channel was formed by directly bioprinting of human umbilical vein endothelial cells (HUVECs) incorporated into the gelatin solution. They confirmed the vascular channel functionality by comparing the diffusional permeability of the vascular channel with a bare channel. The results of this study suggest that the fabricated skin model represents a microenvironment more closely than conventional reconstructed skin models and it can be used as a reliable platform for drug screening, cosmetic testing, and basic research [63].

Although the functionality of the more complex 3D printed or microfluidic models are well confirmed by evaluating cells using differentiation and proliferation markers, their applications are confined to evaluating the effect of new compounds on healthy skin models [69], [70]. There is still a need to develop an infected wound model for studying the healing mechanism, inflammatory responses, and the efficacy of new therapeutic agents.

## 1.4. Conclusion and Objectives

The complex structure of human skin is responsible for critical functions including regulating body temperature, sensation, and protection against radiation, mechanical forces, chemical agents and pathogens. Skin wounds can interfere in these functions and cause more serious physical problems. Studying the wound healing mechanisms and identifying the impediments to wound healing is an important step in optimizing therapeutic agents and drug delivery systems. The ethical issues of using human participants in research studies necessitate finding an alternative model for experimental studies. Currently, skin models including animal and *in vitro* 2D models have been widely used in wound modeling and drug discovery studies. However, several problems such as

the high cost and ethical issues of using animals and non-translatable results to human physiology have brought the researchers' attention to developing *in vitro* 3D skin equivalents representing the human skin behavior in response to stimuli and therapeutic agents. Although several successful *in vitro* 3D human skin models have been developed and the functionality of them confirmed, there is still a substantial need to develop an infected skin wound model for studying the skin healing mechanism, inflammatory response, and drug studies.

In this work, we developed a simplified functional skin model, resembling skin barrier function to use in studying wound infection, proinflammatory response, and drug testing. We started with developing the epidermis layer because it is the main physical barrier in drug delivery and plays an important role in activating the innate immune system when in contact with pathogens (Figure 10). We employed enzymatically crosslinked gelatin to decrease the fabrication cost and enhance the mechanical stability of the construct. In order to facilitate the nutrient delivery to the cells at the air-liquid-interface, a hollow channel resembling a microvessel was created in gelatin by printing Pluronic as a sacrificial material. Keratinocytes, the main cell type of the epidermis, were cultured for 6 weeks, and the terminally differentiated cells formed a multilayer structure. We infected the epidermis model with *Escherichia coli* and studied the proinflammatory response of keratinocytes to infection and drug testing of the antibiotic ciprofloxacin.

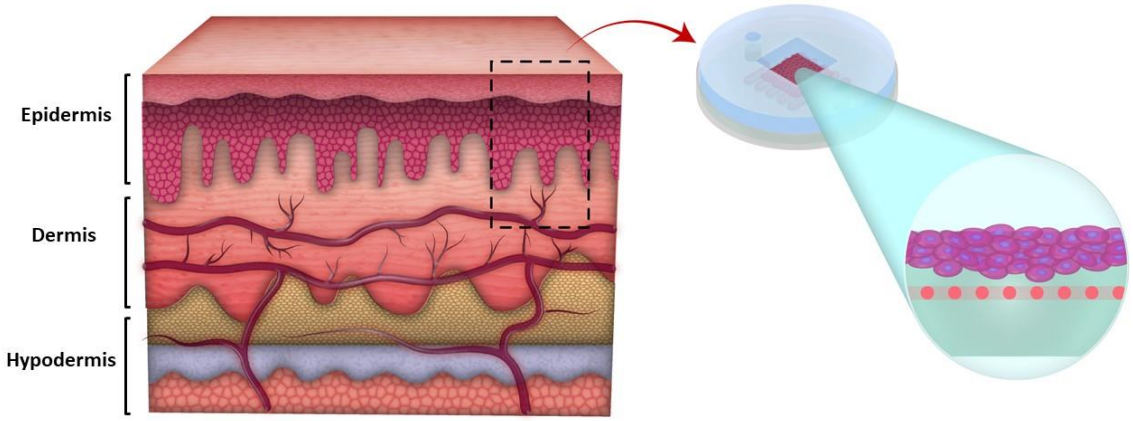


**Figure 10. Simplified skin model including epidermis layer as the first and main barrier of skin and vasculature channel.**

# Chapter 2: Fabrication and Characterization of Gelatin Hydrogel

Tissue engineering scaffolds are designed to create a desirable microenvironment and cellular interactions to support the formation of new functional tissues. Among the biomaterials used for this purpose, ECM proteins such as collagen, elastin, and hyaluronic acid have attracted researchers' attention due to their high capability of mimicking the biological properties of ECM [71].

Gelatin is a denatured form of collagen, which is obtained by controlled hydrolysis of fibrous collagen. Gelatin mainly consists of triple amino acids of glycine, proline, and hydroxyproline. It is used as an additive in different biomaterials to enhance cell–scaffold interactions through its Arg-Gly-Asp (RGD) motifs which are recognized by integrin receptors on cell membranes. Gelatin is more cost-effective and less antigenic than collagen and its tunable mechanical properties enable the fabrication of hydrogels with different degrees of stiffness [71], [72]. The use of gelatin hydrogel in scaffolds for skin tissue engineering has been well established (Table 2) [71].

**Table 2. Gelatin-based scaffolds for skin regeneration application** [71]**.**

| **Biomaterial** | **Fabrication method** | **Cell(s)** | **Performance** |
|---|---|---|---|
| **Gelatin** | SCPL + Freeze-drying +EDC crosslinking | HDF Pre-seeding with fibroblasts | led to a better performance in reepithelialization |
| **Gelatin** | Electrospinning + DHT and EDC crosslinking | HDF, HEK | Inter-fiber distances between 5 and 10 μm results in the best dermis and epidermis organization |
| **Gelatin** | Needleless electrospinning + GA crosslinking | BM-MSCs, HDF, HEK | Faster wound closure, enhanced reepithelialization, increased depth of granulation tissue and density of myofibroblasts in the wound area for gelatin vs PCL |
| **Gelatin–C6S–HA** | Freeze-drying + EDC crosslinking | Foreskin dermal fibroblasts and keratinocytes | Enhanced wound healing and graft take compared to the acellular scaffolds, with a well-developed epidermis and dermal–epidermal junction basement membrane after 4 weeks |
| **Gelatin–C6S–HA** | EDC crosslinking + Freeze-drying | VEGF165-modified rHFSCs | Promotes vascularization in the scaffold and enhances wound healing |
| **Gelatin–fibrinogen** | GA crosslinking + Freeze-thawing | Primary HDF | Cell proliferation and infiltration were affected by GA crosslinker, mostly lower than Integra |
| **Gelatin, collagen (bilayer)** | Freeze-thawing, gelation | Acellular | Promote reepithelialization and wound healing |

The mechanical properties of gelatin can be enhanced with several approaches of crosslinking including physical, chemical, and enzymatical methods. Physical crosslinking of gelatin occurs when gelatin solution cools below 35°C and the random coil gelatin molecules form a triple helix structure of collagen (Figure 11). However, the thermo-responsivity of gelatin limits its applications at physiological temperature (37°C) as it turns back to liquid form [71]. Therefore, other methods of crosslinking such as

photocrosslinking with ultraviolet (UV) light is used to improve the mechanical properties of gelatin hydrogel [73], [74]. Photocrosslinked hydrogels are more mechanically and chemically stable but using photo-initiator agents and UV light exposure result in cell viability reduction. For chemically crosslinking gelatin, there are various chemical reagents including formaldehyde, glutaraldehyde, and genipin. Although chemical reagents are efficient in increasing the stability of gelatin hydrogel, they usually cause cytotoxic effects or immunological responses by host tissue [71], [75].

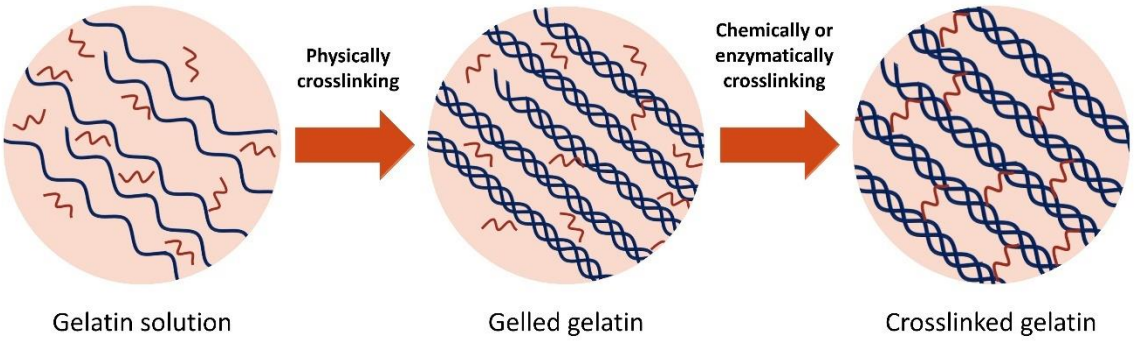


**Figure 11. Schematic picture representative of physically and chemically/enzymatically crosslinking of gelatin.**

Enzymatically crosslinking refers to the use of enzymes such as tyrosinase and transglutaminase for crosslinking gelatin and collagen. Transglutaminase is more common as using it results in a gelatin hydrogel with higher mechanical strength and stability compared to using tyrosinase. Until the discovery of microbial transglutaminase (mTG), the high price of this enzyme had limited its application. mTG is derived from streptomycetes and can be activated independently of $Ca^{2+}$ within a wide range of temperature and pH [75]. mTG catalysescatalyzes the reaction (transamidation) between

the glutamine and lysine groups of gelatins (Figure 12). It has been reported that mTG is non-toxic and causes no side-effects on several cell types [71], [75].

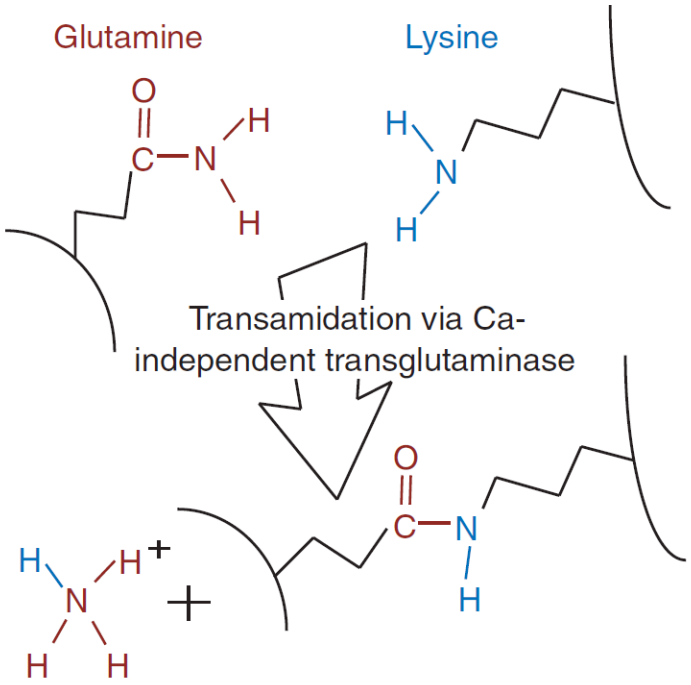


**Figure 12. Glutamine residues in gelatin can be covalently linked to lysine residues via a transamidation reaction that results in the production of ammonia** [76]**.**

## 2.1. materials and methods

### 2.1.1. Preparation of Gelatin Hydrogel

Enzymatically crosslinked gelatin was prepared as described previously [76]. Briefly, gelatin powder from porcine skin (Sigma-Aldrich, USA, Catalog No.: G1890-1KG) was dissolved in Dulbecco's phosphate-buffered saline (DPBS, Sigma-Aldrich, USA, Catalog No.: D8537-500ML) at 60 °C to achieve final gelatin concentrations of 10, 15, and 20% (w/w). Then the solutions were sterilized using 0.22 µm filters. The microbial transglutaminase (mTG, Modernist Pantry, USA) solutions were prepared with different

concentrations of 2.5, 5, and 10 U/mL by dissolving a proper amount of mTG in DPBS and then sterilized using 0.22 µm filter. Gelatin/mTG hydrogels were prepared by mixing mTG solutions with different concentrations of gelatin at 60 °C. Then solutions were incubated at 37 °C for 12 hours to complete crosslinking process.

### 2.1.2. Mechanical Properties Measurement

For optimizing the amount of enzyme, the storage modulus of 15% (w/w) gelatin with various amounts of mTG was measured using the non-destructive method described previously [77]. Briefly, 2 mL of 15% gelatin solutions with 2.5, 5, and 10 U/mL mTG were poured in the detachable sample holder specially designed for ElastoSens™ Bio2 (Rheolution, CA). The real-time storage modulus measurement was performed for 12 hours using the ElastoSens™ Bio2. The same study was conducted for measuring the storage modulus of 10, 15, 20% (w/w) gelatin hydrogels with 5 U/ml mTG. Using the device, for each sample, the storage modulus was measured 3 times every 5 minutes. Samples were prepared in 3 replicates for each condition.

### 2.1.3. Swelling Ratio

Gelatin hydrogel disks were prepared in three replicates for each concentration as explained in section 2.1.1 and freeze-dried. Then, they were weighed (Wd) and incubated in DPBS at 37 °C for 24 hours. At each time point, they were removed from DPBS, lightly blotted and weighed (Ws). The swelling ratio of the swollen gel was calculated according to Equation (1) [73].

$$\text{Swelling Ratio}\,(\%) = \frac{Ws - Wd}{Wd} \times 100 \quad (1)$$

### 2.1.4. *In Vitro* Enzymatic Degradation

For studying the degradation rate of gelatin hydrogels, gelatin disks with 1.5 cm diameter were prepared in three replicates as mentioned in section 2.1.1. After gelation, the hydrogels were weighed ($W_0$) and immersed in 2 mL of 2 U/mL collagenase (Sigma-Aldrich, USA, Catalog No.: LS004174) solution in 12-well plates and incubated at 37 °C. Weight measurements were performed ($W_t$) every 24 hours for 20 days. The collagenase solutions were refreshed every 2 days. Finally, the degree of degradation was plotted as the percentage of the remaining hydrogel mass versus the initial hydrogel mass according to Equation (2) [73].

$$\text{Mass Remaining (\%)} = \frac{W0-Wt}{W0} \times 100 \quad (2)$$

### 2.1.5. Mechanical Stability of Gelatin Hydrogel in Culture

In order to examine the mechanical behaviors of gelatin hydrogels in culture, immortalized human keratinocytes (HaCaTs, Addexbio, USA, Catalog No.: T0020001) were seeded with the seeding density of 50,000 cells/cm$^2$ onto the hydrogels prepared in the detachable sample holder specially designed for ElastoSens Bio2 as explained in section 2.1.2. Subsequently, the samples were incubated at 37 °C and 7% CO2 for cell attachment for 24 hours. The ElastoSens device was used for measuring the storage modulus of hydrogels over 14 days of culture. The storage modulus was measured 3 times every 5 minutes. Samples were prepared in 3 replicates for each gelatin concentration.

### 2.1.6. Scanning Electron Microscopy

Scanning electron microscopy (SEM) was used to visualize the morphology of gelatin. For this purpose, the lyophilized hydrogels were mounted on the SEM stub and coated with

gold-palladium hummer sputter (Hummer VI sputter coater, Anatech, USA). SEM images were obtained by a Hitachi electron microscope (Hitachi S4800, Japan) with 1.0 kV voltage.

### 2.1.7. Cell Attachment and Cell Number

Gelatin/mTG solutions with various gelatin concentrations (10, 15, and 20%) were prepared as described above. After incubating the hydrogels with Dulbecco's Modified Eagle Media (DMEM, Gibco™ by Life Technologies™, USA, Catalog No.: 11965092) with 10% fetal bovine serum (Gibco™ by Life Technologies™, USA, Catalog No.: 10437036) for 12 hours, HaCaTs were seeded onto the gelatin hydrogels with the seeding density of 50,000 cell/$cm^2$. After 24 hours of incubation at 37 °C in the incubator with 7.2% $CO_2$, cells were stained with a live/dead viability kit to assess cell adhesion by measuring the percentage of cell-covered area. In order to stain the samples, hydrogels were washed three times with sterile DPBS and incubated at room temperature for 30 minutes in a solution with the concentration of 2 μM Calcein—AM (Invitrogen, USA, Catalog No.: L3224) and 4 μM ethidium homodimer (EthD-1, Invitrogen, USA, Catalog No.: L3224) in DPBS. After incubation, the samples were washed with DPBS and then images were obtained by ZEISS confocal microscope (Zeiss LSM880, ZEISS, Oberkochen, Germany). Additionally, ImageJ software (National Institutes of Health, USA) was used for determining the cell-covered area. The similar staining procedure was utilized on days 1, 4, and 7 to determine the cell number. Samples were prepared in 3 replicates for each gelatin concentration.

### 2.1.8. Cell morphology

To study the morphology of HaCaT cells on gelatin hydrogels, the samples were prepared as described in section 2.1.7 and after 24 hours incubation, cells were fixed with 3.7% (v/v) formaldehyde (VWR, USA, Catalog No.: 10790710) for 15 minutes. Then cells were washed with PBS and permeabilized with 0.1% (v/v) Triton X-100 (BIO BASIC, USA, Catalog No.: TB0198) solution for 15 minutes. Afterward, the samples were washed with PBS and incubated with 0.5% DAPI (Sigma-Aldrich, USA, Catalog No.: D9542) and 0.1% Alexa Fluor™ 488 Phalloidin (Invitrogen, USA, Catalog No.: A12379) solution in PBS for 30 minutes. Finally, the samples were washed and imaged using a Zeiss confocal microscope (Zeiss LSM880, ZEISS, Oberkochen, Germany) with 20 x magnification objectives

### 2.1.9. Cell Proliferation

In order to evaluate cell proliferation on different concentrations of gelatin, the samples prepared as described above. Then they were incubated with media containing PrestoBlue reagent (Invitrogen, USA, Catalog No.: A13262) with 9:1 ratio for 45 minutes at 37 °C on days 1, 4, and 7. Afterward, 100 µl of supernatants were collected from each well and the fluorescence intensity was measured at excitation wavelengths of 560 nm and emission of 590 nm using a microplate reader (Infinite M Nano, Tecan, Switzerland). Relative proliferation rate was calculated by normalizing the measured intensity of each condition ($I_t$) with respect to the blank ($I_b$) and dividing by the lowest intensity on day 1 ($I_{min}$-$I_b$) according to Equation (3).

$$\text{Relative Fluorescence Unit} = \frac{It - Ib}{Imin - Ib} \quad (3)$$

### 2.1.10. Statistical Analysis

Results were analyzed by GraphPad Prism version 8 (GraphPad Software, La Jolla, CA). Statistical significance was analyzed using one-way ANOVA for more-than-two-group comparisons with one independent variable and two-way ANOVA for more-than-two-group comparisons with two independent variables.

## 2.2. Result and discussion

### 2.2.1. Mechanical Properties of Gelatin

To crosslink gelatin enzymatically, transglutaminase was added to the gelatin solutions to obtain a biocompatible hydrogel [76]. Transglutaminase catalyzes the formation of a covalent bond between the carbonyl (Glutamine) and amino (Lysine) groups in gelatin. Crosslinking kinetics of 15% (w/w) gelatin/mTG was studied as a function of mTG concentration by real-time measuring of storage modulus (G′) over a period of 12 hours. The storage modulus represents the elastic portion of the viscoelastic behavior and explains the solid-state behavior of the hydrogel [78]. G′ is used as an indicator of mechanical strength and shows the gradual transformation of gelatin from solution state to gel. Results show that storage modulus continuously increased in all samples with different mTG concentrations, while a higher level of storage modulus (28.2±3.4 kPa) was observed as the concentration of mTG increased to 10 U/mL which is due to a greater extent of crosslinking (Figure 13). However, 10 U/mL mTG is associated with localized fast gelation and difficulties in sample manipulation, therefore, 5 U/mL mTG was selected for the remaining experiments.

Results from studying the effect of gelatin concentration with 5 U/mL mTG on the storage modulus of the hydrogels are shown in Figure 14. It was observed that hydrogels

with 20% (w/w) gelatin concentration had the highest storage modulus (29.5±1.3 kPa) due to the higher density of carbonyl and amino groups available for bonding to each other.

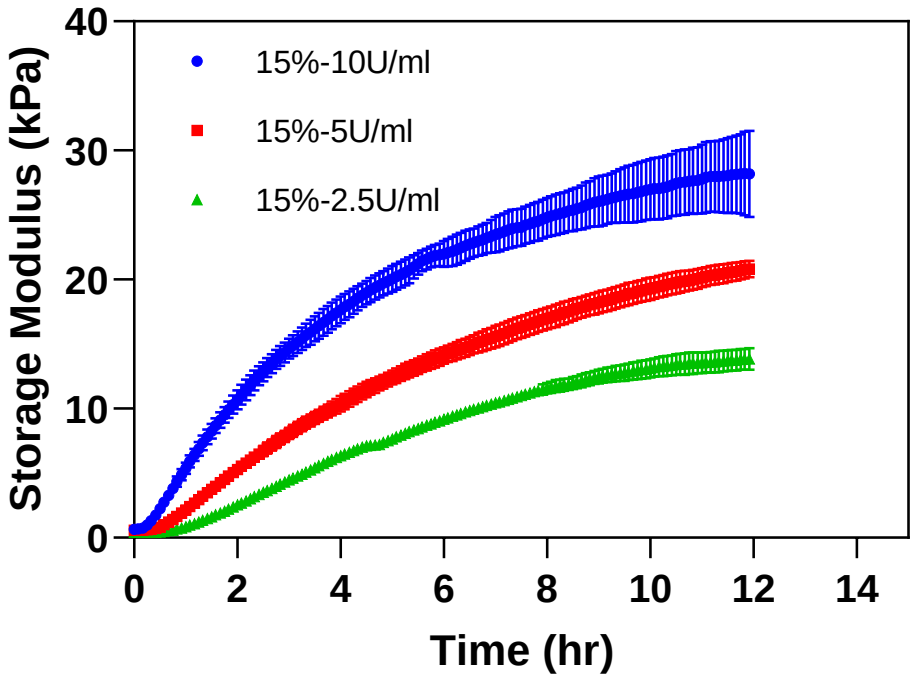


**Figure 13. Storage modulus of 15% gelatin crosslinking with 2, 5, and 10 U/mL of mTG. Error bars indicate standard deviation (n=3).**

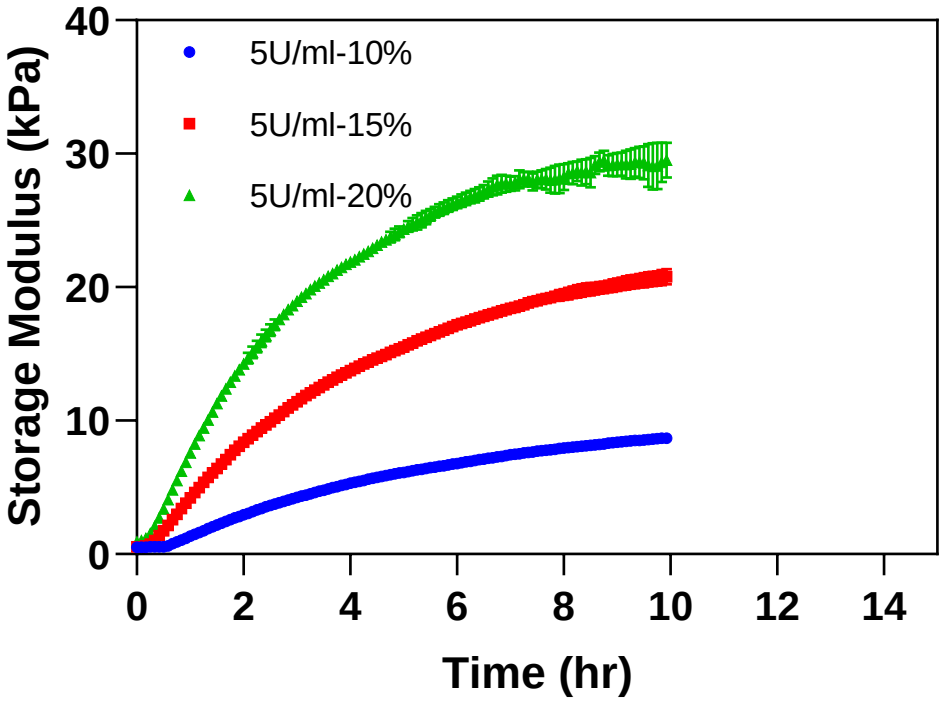


**Figure 14. Storage modulus of 10, 15, and 20% gelatin with 5 U/mL of mTG. Error bars indicate standard deviation (n=3).**

Following the completion of crosslinking after about 12 hours, the complex ($G^*$) and loss ($G''$) moduli of the hydrogels were measured (Figure 15). The loss modulus represents the viscous portion of the viscoelastic behavior and describes the liquid-state behavior of the hydrogel. Results show that at all concentrations, the hydrogels showed dominant solid-state behavior ($G' > G''$). This is due to covalent bonds within the gelatin triple helixes.

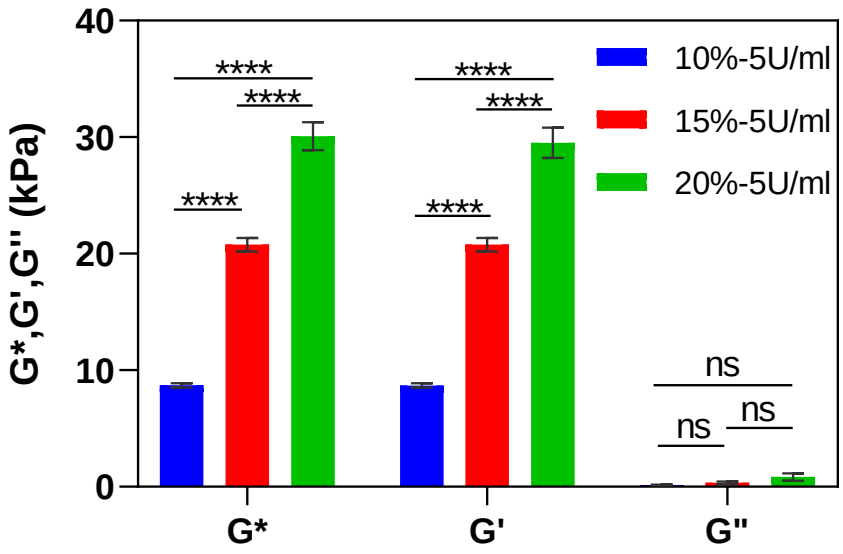


**Figure 15. Summary of mechanical properties of 10, 15, and 20% gelatin hydrogels after crosslinking with 5 U/mL mTG. $G^*$, G′, and G″ are representative of complex, storage, and loss modulus respectively. Error bars indicate standard deviation (n=3, ns and **** indicate nonsignificant and $p<0.001$ respectively).**

### 2.2.2. Swelling Ratio

The swelling ratio of the hydrogels governed by the osmotic pressure is important as it affects solute diffusion, surface properties, and mechanical properties and stability [74]. The swelling ratio is affected by the pore size of the polymer network which is a function of gelatin concentration. To study the effect of gelatin concentration on swelling ratio, dried hydrogels with different gelatin concentrations were immersed in PBS solution and weighed at each time point. As it is shown in Figure 16, all gelatin concentrations offered a high swelling capacity while the 10% gelatin hydrogel had a significantly higher swelling ratio (600%) than 15 and 20% hydrogels.

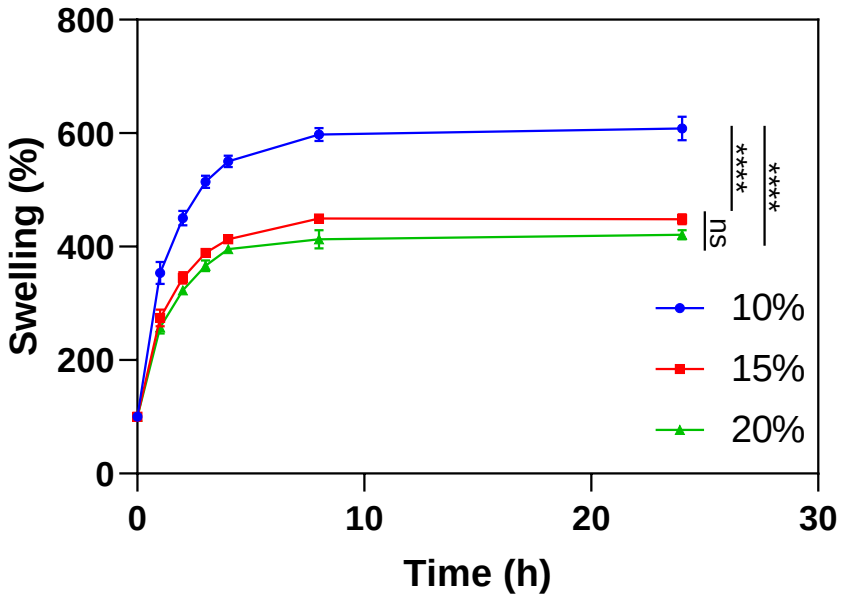


**Figure 16. Swelling ratio of 10, 15, 20% gelatin hydrogels. Error bars indicate standard deviation (n=3, ns and **** indicate nonsignificant and $p<0.001$ respectively).**

### 2.2.3. *In Vitro* Enzymatic Degradation

To study the degradation rate, gelatin hydrogel disks with 15 mm diameter and 7 mm thickness were incubated with 2 U/mL collagenase solution at 37°C. Figure 17 shows a continuous weight loss in all samples due to the cleavage of peptide bonds within the gelatin structure. The results demonstrated that an increase in the gelatin concentration reduced the degradation rate. The full dissolution of hydrogels enhanced from 7 days in 10% gelatin to 14 and 18 days for 15% and 20% gelatins, respectively. The higher swelling ratio of the 10% gelatin accounts for the quick uptake of the collagenase by the hydrogel. This event results in increasing the contact surface of hydrogel with enzyme and accelerating the degradation process. The higher crosslinking density is the main cause of the lower swelling ratio and the prolonged degradation of the 20% gelatin.

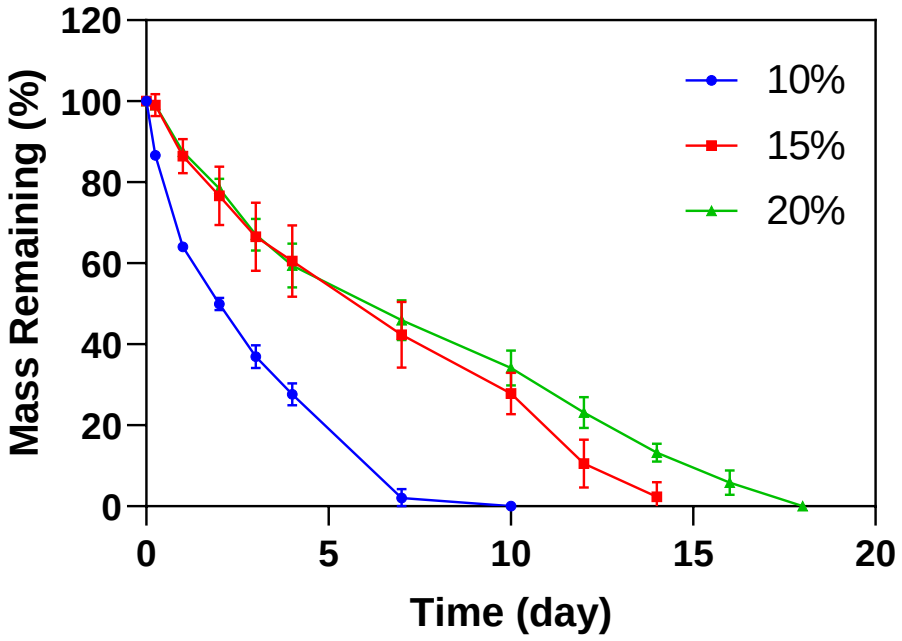


**Figure 17. Mass remaining percentage of 10, 15, and 20% gelatin hydrogels during degradation in 2 U/mL collagenase. Error bars indicate standard deviation (n=3).**

### 2.2.4. Mechanical Stability of Gelatin Hydrogel in Culture

In order to examine the stability of cell-seeded gelatin hydrogels and determine the impact of cell-secreted materials on the integrity of hydrogels, HaCaT cells with a density of 50,000/cm$^2$ were seeded on the hydrogels. The storage modulus was then measured at different time points (Figure 18). The results show that 10% gelatin lost its mechanical stability after 7 days of incubation and detached from the measuring containers. For 15% gelatin, the hydrogel maintained its integrity for 14 days although its storage modulus decreased by 50%. The 20% gelatin hydrogel, on the other hand, maintained its integrity over 14 days of incubation with no reduction in its storage modulus.

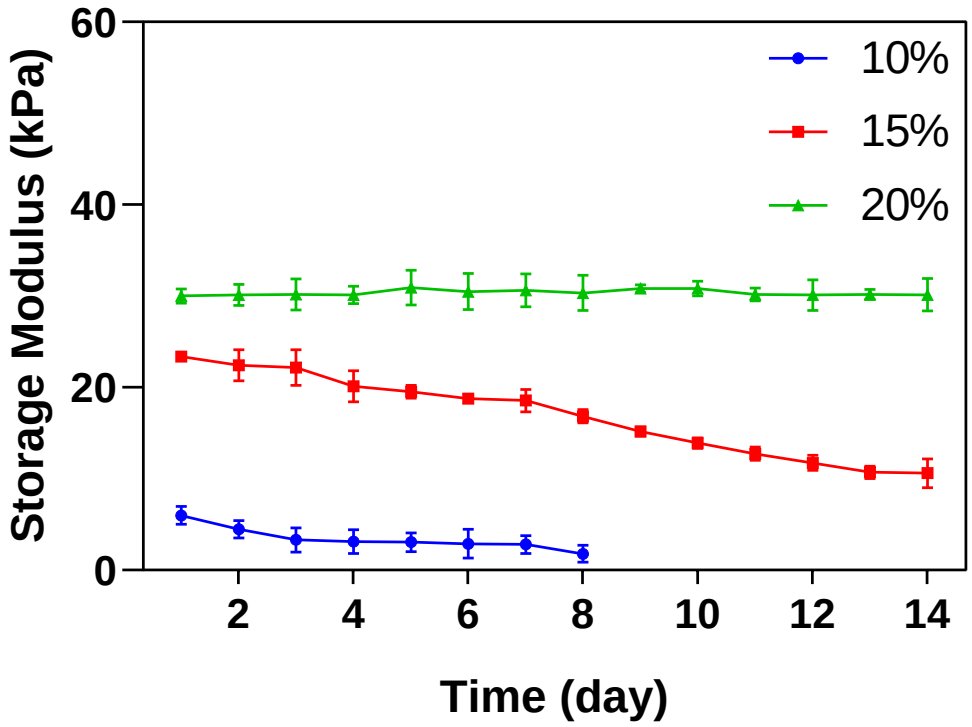


**Figure 18. Storage modulus of 10, 15, and 20% gelatin hydrogels during cell culture. Error bars indicate standard deviation (n=3).**

### 2.2.5. Scanning Electron Microscopy of Gelatin Hydrogel

Microstructural analysis of the hydrogels was performed using scanning electron microscopy (SEM) which is shown in Figure 19. The images show that increasing the concentration of gelatin resulted in the reduction of pore sizes. The superior mechanical properties of 20% gelatin can also be attributed to the smaller pore size observed within the hydrogel (Figure 19 C). These results suggest that mechanical properties and biodegradability of these hydrogels can be tuned by changing the concentration of gelatin and subsequently the extent of crosslinking degree.

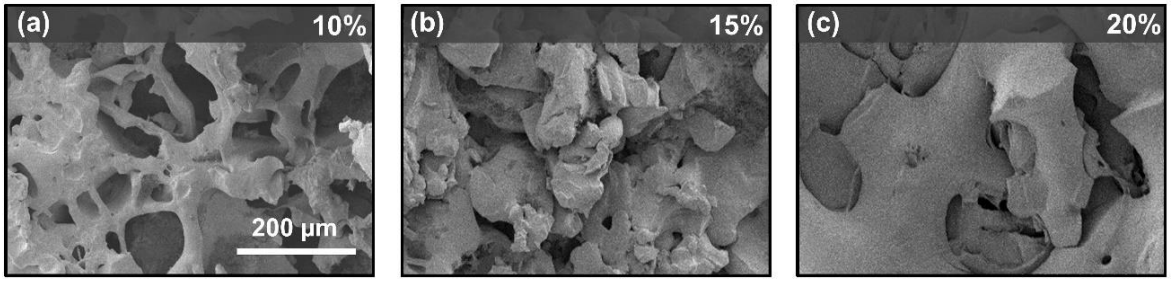


**Figure 19. SEM images of hydrogels with 10% (a), 15% (b), and 20% (c) gelatin concentrations.**

### 2.2.6. Cell Viability and Attachment on Gelatin Hydrogels

In order to evaluate the capability of the hydrogels in maintaining cell viability and promoting cell proliferation, experiments were performed by culturing HaCaT cells which previously shown to have well-established *in vitro* differentiation and proliferation capabilities [36], [73], [79]. HaCaT cells were seeded on gelatin hydrogels with 10, 15, and 20% concentration. Cell viability was studied by staining cells using a live/dead staining kit showing the live cells in green and dead ones in red (Figure 20). It was observed that in three different concentrations of gelatin over 95% cell viability was achieved, which reveals the biocompatibility of hydrogels in this range of gelatin concentration.

Moreover, measuring the cell covered area by ImageJ software on day 1 shows that 60% of the surface of 20% (w/w) gelatin is covered by HaCaT cells while in 15 and 10% (w/w) gelatins the cell covered area is about 40% (Figure 21). This could be a result of the higher number of available cell-binding sites (RGD) provided by higher concentrations of gelatin [71], [72].

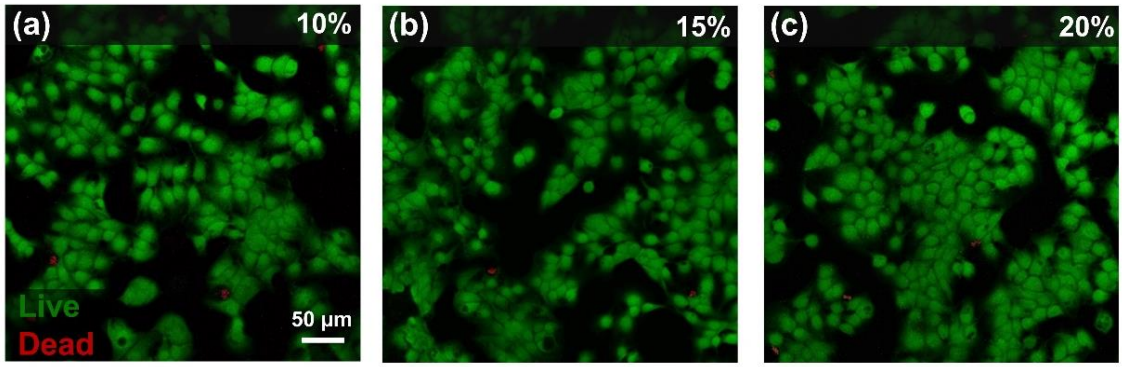


**Figure 20. Representative live/dead fluorescence images of HaCaT cells on gelatin surfaces of 10% (a), 15% (b), and 20% (c) after 1 day of culture. Green fluorescent cells are alive and red fluorescent cells indicate dead ones.**

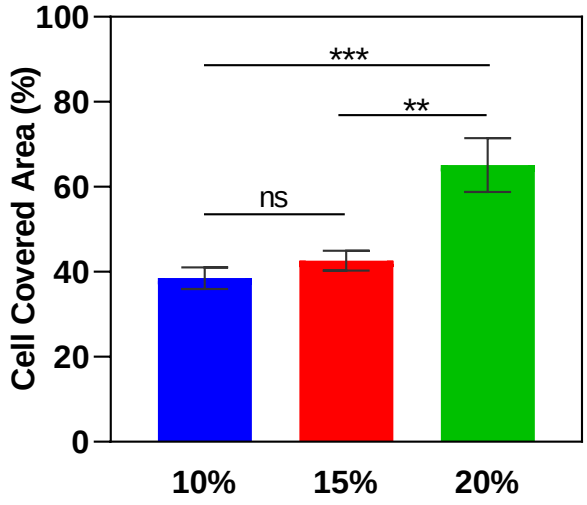


**Figure 21. Quantification of cell covered area of 10, 15, and 20% gelatin hydrogels on day 1 using NIH ImageJ software. Error bars indicate standard deviation (n=3, ns, **, and *** indicate nonsignificant, $p<0.01$, and $p<0.001$ respectively).**

### 2.2.7. Cell Morphology on Gelatin Hydrogels

To study the morphology of HaCaT cells on gelatin hydrogels, the actin filaments as a key cytoskeletal protein was stained with phalloidin. The obtained images showing the

actin filaments in green and nuclei in blue confirmed the tightly packed morphology of HaCaT cells on all gelatin concentrations (Figure 22). This result demonstrates that these gelatin concentrations do not affect cell morphology.

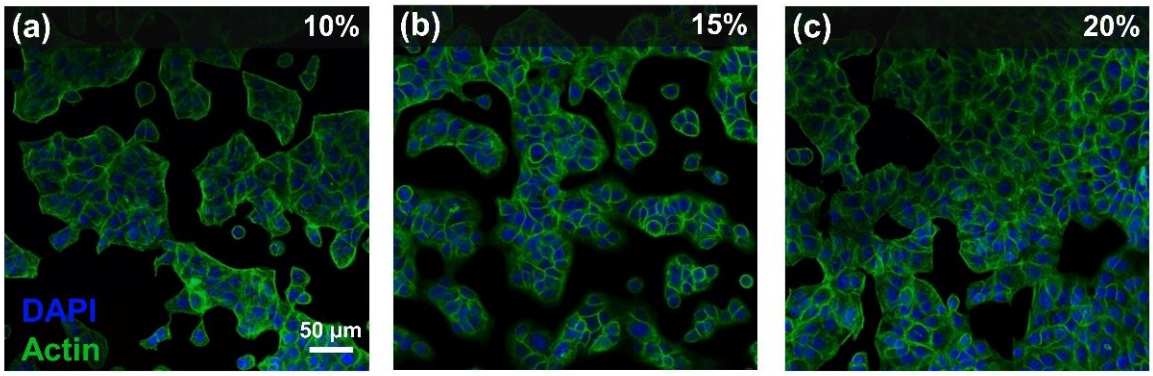


**Figure 22. Representative phalloidin/DAPI fluorescence images of HaCaT cells on gelatin surfaces of 10% (a), 15% (b), and 20% (c) after 1 day of culture. Cell filaments are stained by phalloidin (green) and nuclei stained by DAPI (blue).**

### 2.2.8. Cell Number and Proliferation

The number of live cells on the hydrogels were counted on days 1, 4, and 7 to evaluate the proliferation in a unit area. Results show that the number of HaCaT cells on 15 and 20% (w/w) gelatin hydrogels on days 4 and 7 is significantly higher than cells on 10% (w/w) gelatin. (Figure 23) This implies that mechanical properties of the gelatin hydrogel not only affect the cell attachment but also it can significantly affect the HaCaT proliferation. This result demonstrates that HaCaT cells tend to proliferate more on hydrogels with higher gelatin concentration and stiffer surfaces.

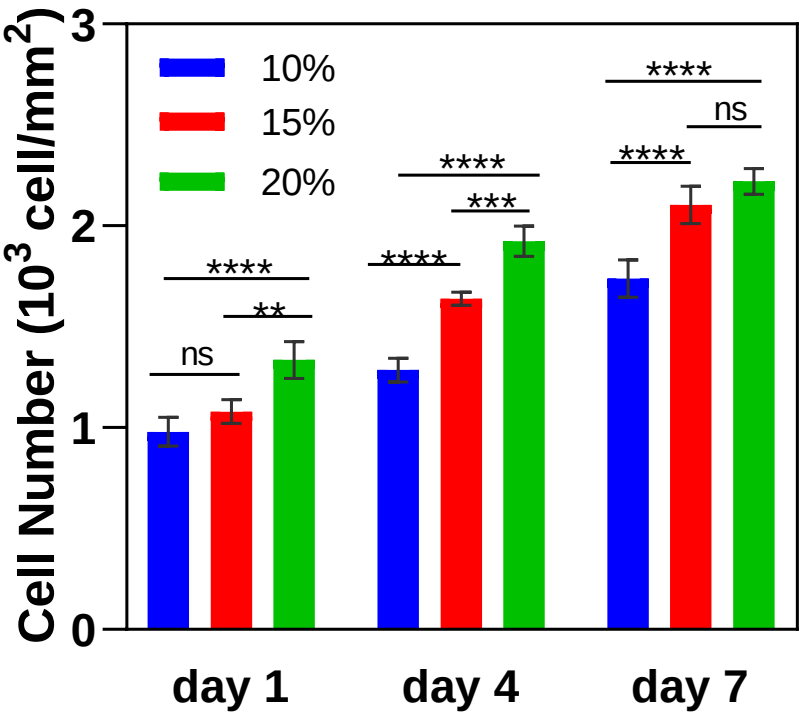


**Figure 23. Quantification of live cells using live/dead fluorescence images of HaCaT cells on 10, 15, and 20% gelatin hydrogels on days 1, 4, and 7. Error bars indicate standard deviation (n=3, ns, **, ***, and **** indicate nonsignificant, *p*<0.01, p<0.001, and *p*<0.0001 respectively)**

To confirm the cell number data, the metabolic activity of HaCaT cells was investigated using the PrestoBlue cell viability reagent. After a 45-minute incubation of cells with PrestoBlue, the relative fluorescence intensity of the supernatants confirms a higher proliferation rate for 15 and 20% (w/w) gelatin hydrogels compared to 10% (w/w) gelatin (Figure 24).

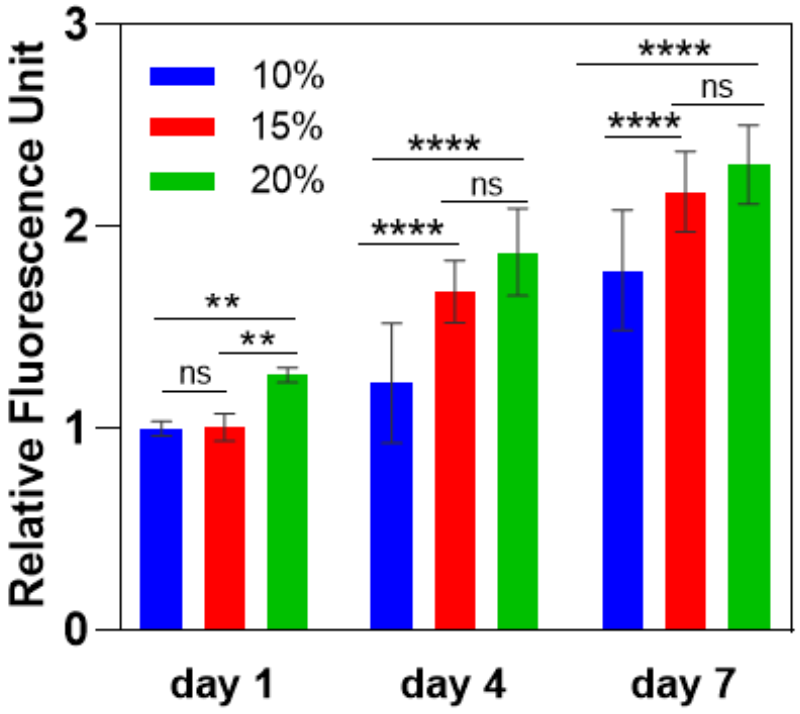


**Figure 24. Cell proliferation of HaCaT cells on 10, 15, and 20% gelatin hydrogels indicated by relative fluorescence unit using PrestoBlue Cell Viability Reagent. Error bars indicate standard deviation (n=10, ns, **, and **** indicate nonsignificant, $p<0.01$, and $p<0.0001$ respectively)**

## 2.3. Conclusion

Gelatin is a well-known biomaterial for skin tissue engineering. However, the approach of crosslinking can affect the biocompatibility and mechanical properties of the resulting hydrogel. Among the existing gelatin crosslinking methods, enzymatically crosslinking processes are highlighted due to the minimum adverse effects on hydrogel biocompatibility as well as providing the hydrogel with suitable mechanical properties and stability for tissue engineering applications. The results showed that the storage modulus as an indicator of the mechanical stability of the gelatin hydrogel increases by increasing the gelatin

concentration. The higher number of available carbonyl and amino groups in higher gelatin concentration accounts for the greater extent of crosslinking degree and higher storage modulus. This can directly result in less porosity and swelling capacity and also a slower degradation rate in hydrogels with higher gelatin concentration. Considering both physical properties and cytocompatibility of the studied gelatin hydrogels, 20% (w/w) gelatin hydrogel was selected for developing the final model due to its superior capacity for supporting cell attachment and proliferation. Moreover, its relatively slower degradation rate makes it a suitable option for long-term differentiation of HaCaT cells to a functional epidermis tissue.

# Chapter 3: Model Development and Epidermis Tissue Formation

In 1986, 3D printing was first introduced by Charles W. Hull as an additive manufacturing approach which has led to significant innovations in many areas including science, industry, and education. He was successful in producing a solid 3D structure by curing the sequentially printed layers with UV light. This process was a basis for creating sacrificial molds for the formation of 3D structures from biological materials [80]. Recent advances in 3D printing approaches have facilitated the printing of not only biological materials but also living cells to create complex 3D functional living tissues (Figure 25 A) [80], [81]. The main 3D bioprinting techniques including inkjet, laser-assisted, extrusion printing, and stereolithography, have several advantages including accurate control of cell distribution, high resolution, scalability, and cost-effectiveness. However, currently, there is no single bioprinting technique offering all these advantages simultaneously [81].

Inkjet bioprinting was the first method of bioprinting and it is still the most commonly used printing technique for both biological and nonbiological materials. In this technique, thermal or piezoelectric actuators deform the printer head and lead to deposition of droplets in controlled volumes in a predefined pattern (Figure 25 B) [80], [81]. Inkjet bioprinting provides high printing speed and relatively high cell viability (80-90% according to experimental results) with low cost (Table 3). However, using the micro-electromechanical system (MEMS) in its printer heads has limited its applications to bioinks with low viscosity (>15 mPa/s) and low cell density. High cell density results in increasing the average viscosity of bioinks and clogging of the printer heads [81].

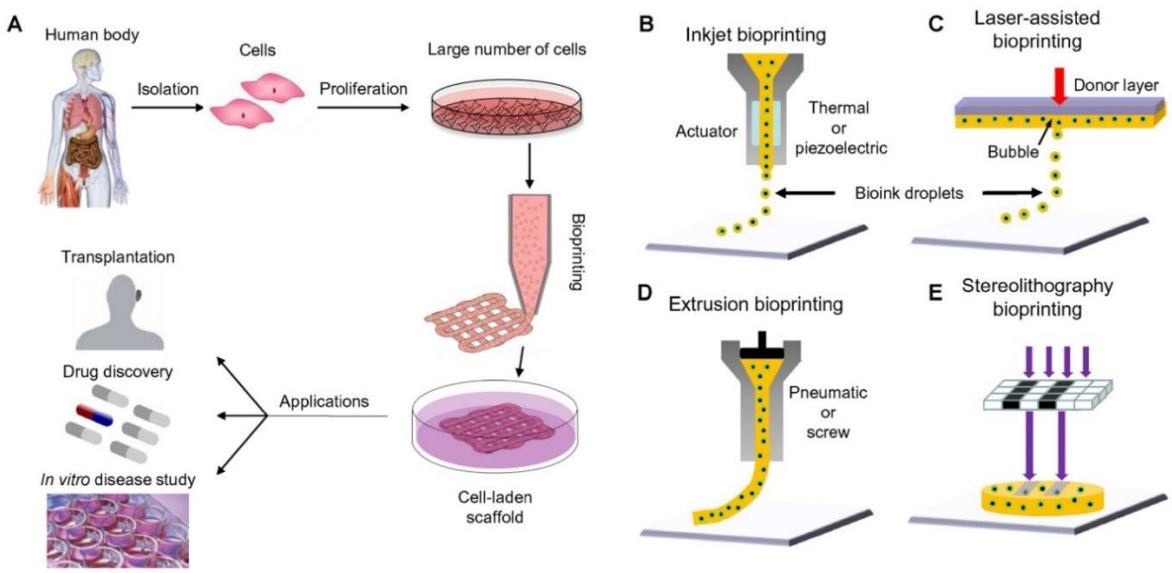


**Figure 25. Bioprinting process, techniques, and applications. A) For human therapeutic applications, the typical workflow of bioprinting would involve the isolation and expansion of human cells prior to printing the desired cell-laden scaffold. B) Inkjet printers eject small droplets of cells and hydrogel sequentially to build up tissues. C) Laser bioprinters use a laser to vaporize a region in the donor layer (top) forming a bubble that propels a suspended bioink to fall onto the substrate. D) Extrusion bioprinters use pneumatics or manual force to continuously extrude a liquid cell–hydrogel solution. E) Stereolithographic printers use a digital light projector to selectively crosslink bioinks plane-by-plane. In (C) nd (E), colored arrows represent a laser pulse or projected light, respectively** [81]**.**

Laser-assisted bioprinting has been established on principles of laser-induced transfer [80], [81]. The laser-assisted bioprinter is composed of a pulsed laser beam, focusing system, ‘ribbon’ and receiving substrate [80]. The ‘ribbon’ has a donor layer on the top which is responsive to laser stimulation, an energy-absorbing layer like titanium or gold, and bioink solution layer on the bottom. The focused laser plus is used to stimulate a specific area on the absorbing layer. During this process, a portion of the donor layer vaporizes and makes a high-pressure bubble at the bioink layer interface. This high-pressure bubble pushes a bioink droplet to the receiving substrate. The falling bioink

droplet becomes crosslinked when it reaches the substrate (Figure 25 C) [81]. Laser-assisted printing has several advantages over inkjet printing (Table 3). In this method, there is no direct contact between the dispenser and the bioink which results in the elimination of mechanical stress on the cells and subsequently increasing the cell viability (usually higher than 95%). Moreover, using laser-assisted printers enables printing a wider range of biomaterials with higher viscosity and cell density. However, the laser diodes with high resolution and intensity are expensive and the adverse effects of laser exposure on the cells are not yet comprehensively studied [80], [81].

**Table 3. Comparison of four types of 3D bioprinting techniques** [81]**.**

| **Parameters** | **Inkjet Laser** | **Laser-assisted** | **Extrusion** | **Stereolithography** |
|---|---|---|---|---|
| **Cost** | Low | High | Moderate | Low |
| **Cell viability** | >85% | >95% | 40%–80% | >85% |
| **Print speed** | Fast | Medium | Slow | Fast |
| **Supported viscosities** | 3.5 to 12 mPa/s | 1 to 300 mPa/s | 30 mPa/s to above $6 \times 10^7$ | No limitation |
| **Resolution** | High | High | Moderate | High |
| **Cell density** | Low $<10^6$ cells/mL | Medium $<10^8$ cells/mL | High (cell spheroids) | Medium $<10^8$ cells/mL |

Extrusion printing has emerged by modification of inkjet printing techniques in order to print more viscous materials [81]. The ability to print a very wide range of materials and the affordable price have made the extrusion printers the most common 3D printing method [80]. In this technique, an air-force pump or mechanical screw plunger is used to deposit bioinks (Figure 25 D) and by applying a continuous force it is able to print uninterrupted cylindrical fibers instead of single droplets. The extrusion based bioprinter is compatible

with different crosslinking methods including using UV light, chemical agents, or thermal treatments [81]. Additionally, it is able to print bioinks with a very high cell density [80]. However, printing viscose bioinks with higher cell density requires a higher extrusion pressure which causes larger mechanical stresses on cells and reduces the cell viability (40-80%) [80], [81].

Stereolithography bioprinters are composed of a digital light projector to selectively crosslink the bioink layer-by-layer and a movable stage in the vertical direction (Figure 25 E). In this technique, the entire pattern in one layer is printed in one-time exposure which reduces the total time of printing for complex designs. Moreover, controlling the printing stage in only one direction (vertical) simplifies the printing method and increasing the resolution [81].

In this work, an extrusion-based 3D printer has been used to print Pluronic F127 as a sacrificial material to create a hollow channel inside the gelatin hydrogel (Figure 26). Pluronic F127 is a thermo-responsive hydrogel and one of the best printable hydrogels due to the nature of micellar-packing gelation, which allows it to be printed easily and maintain its shape. Moreover, the broad range of its sol-gel transition temperature (10 – 40 °C) allows its viscosity to be stable at both room and human body temperature. [82] Due to such properties, pluronic F127 was selected as a sacrificial material to form the hollow channel with a diameter of 500-800 µm inside the gelatin.

To form the multilayer structure of the epidermis, HaCaT cells were seeded on the gelatin and cultured (submerged culture) for 7 days to form a confluent monolayer. Then, the media was removed from the seeding zone and the differentiation media was delivered to

the cells through the artificial vasculature to culture the cells at the air-liquid interface. (Figure 26)

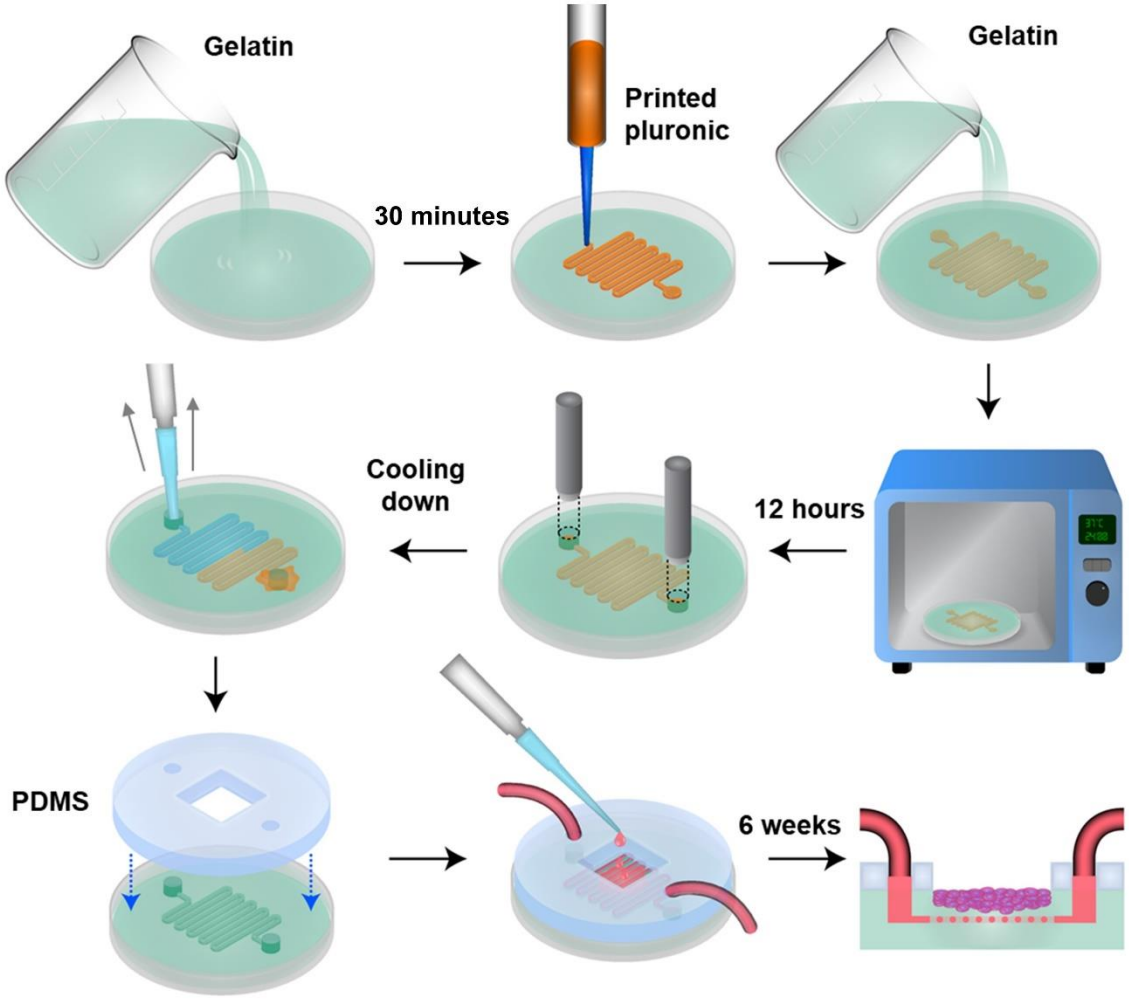


**Figure 26. Model development process. Gelatin/mTG solution was loaded into a 35 mm petri dish. After partial gelation, 38% pluronic F127 solution was printed on the gelatin layer using an extrusion-based 3D printing. Then, another layer of gelatin/mTG solution was poured on the printed pattern and the hydrogel was incubated at 37 °C for 12 hours. An inlet and outlet were created onto the hydrogel using a 5 mm biopsy punch. Afterward, the hydrogel was cooled down to remove the liquid pluronic from the channel. Then, a sterilized PDMS mold was mounted on the gelatin hydrogel to confine the seeding surface to a 1cm×1cm area above the printed channels. Then, HaCaT cells were cultured at air-liquid-interface for 6 weeks to form the multilayer structure of epidermis.**

## 3.1. Methods and materials

### 3.1.1. Model Development

We have developed a novel gelatin-based epidermis model with artificial vasculatures embedded into the gelatin substrate (Figure 27). To fabricate the vasculature-embedded hydrogel, a layer of 20% gelatin was loaded into a 35 mm petri dish. After 30 minutes of incubation at room temperature, 38% Pluronic F-127 (Sigma-Aldrich, USA, Catalog No.: P2443-250G) solution was printed onto the gel as a sacrificial material using a 3D printer (CELLINK+, Gothenburg, Sweden) with 280 kPa pressure. Immediately after printing the pattern, another layer of gelatin was poured onto the construct and the hydrogel was incubated at 37 °C for 12 hours. Afterward, the inlet and outlet were created onto the device using a 5 mm biopsy punch. Subsequently, the hydrogel was cooled down and the liquid Pluronic was removed from the outlet with a pipette to create a hollow channel. Eventually, a UV-sterilized Polydimethylsiloxane (PDMS) mold was mounted on the hydrogel to confine the seeding area to the surface above the printed channel (so-called seeding zone).

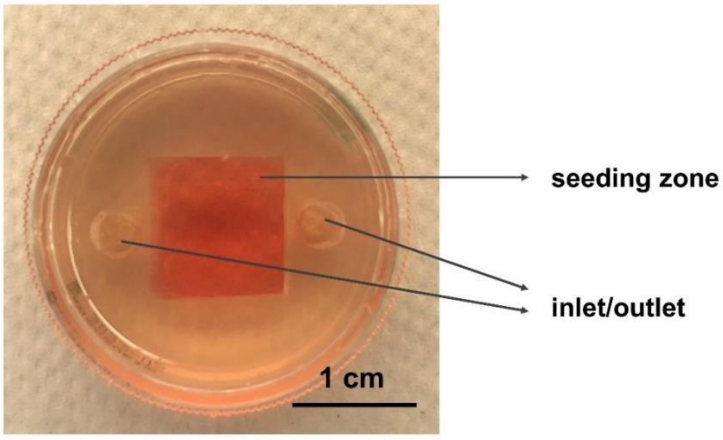


**Figure 27. A prototype of the fabricated model.**

### 3.1.2. Gelatin Hydrogel Permeability

To show the permeability of gelatin hydrogel in nutrient delivery from the channel to HaCaT cells, the diffusion rate of 70 kD FITC-Dextran (Sigma-Aldrich, USA, Catalog No.: 46945-100MG-F) was measured by live imaging. To this end, a 2 mg/mL solution of FITC-Dextran was loaded into the model's channel under an Axio Observer ZEISS microscope (ZEISS, Oberkochen, Germany). Images were taken at 15 minutes intervals for 5 hours. Samples were prepared in 3 replicates.

### 3.1.3. Cell Tight Junction Analysis

To characterize the formation of tight junctions after 7 days of submerged culture, the cells were immunostained with E-cadherin and imaged. Briefly, cells were fixed with 3.7% (v/v) formaldehyde solution for 15 minutes, the samples were incubated with blocking buffer (5% bovine serum albumin and 0.3% Triton X-100 in PBS) for 60 min at room temperature. After washing the samples with PBS, they were incubated with E-Cadherin antibody dilution buffer (Rabbit mAb Alexa Fluor® 488 Conjugate, Cell Signaling Technology, CA, Catalog No.: 3199S) at 4 °C overnight. Subsequently, the samples were incubated with DAPI solution (5 µg/mL) for 15 min at room temperature. The cells were then washed with PBS and imaged using a Zeiss confocal microscope with 20 x magnification.

### 3.1.4. *In Vitro* Epidermis Tissue Formation

HaCaT cells were seeded onto the seeding zone with a density of 50,000 cells/cm$^2$. After 7 days, when the cells reached confluency, the differentiation process was induced as described previously [43]. Briefly, the media was removed, and the cells were left at the air-liquid interface. The differentiation serum-free media composed of DMEM, 1.8 mM

$Ca^{2+}$ (Sigma-Aldrich, USA, Catalog No.: C7902), 2 ng/mL TGF-α (Sigma-Aldrich, USA, Catalog No.: GF022), and 100 ng/mL GMCSF (R&D Systems, CA, Catalog No.: 215-GM-010/CF) was delivered to the cells through the channel.

### 3.1.5. Protein Expression of Developed Epidermis Tissue

Differentiation of HaCaTs was studied by immunostaining of the epidermis cross-sections with filaggrin antibody (terminally differentiation marker) and imaged. To prepare the cross-sections, the epidermis model was fixed with a 3.7% (v/v) formaldehyde solution for 15 minutes, then left in a 30% sucrose solution overnight at 4° C. Then, the hydrogel was mounted in optimal cutting temperature (OCT) compound and froze using liquid nitrogen prior to cryostat sectioning. 5 µm sections were collected on positively charged glass slides. Then the sections were permeabilized using 0.5% Triton X-100 in PBS solution for 5 minutes at room temperature. After 3 times washing with PBS, samples were blocked using 5% normal goat serum albumin solution for 1 hour at room temperature. Then, they were incubated with filaggrin antibody dilution buffer (Mouse mAb Alexa Fluor® 488 Conjugate, Novus Biologicals, CA, Catalog No.: NBP2-54366AF488) at 4 °C overnight. Subsequently, the samples were incubated with DAPI solution (5 µg/mL) for 15 min at room temperature. The samples were then washed with PBS and imaged using confocal microscopy.

### 3.1.6. *In Vitro* Epidermis Electrical Resistance

For measuring the electrical resistance of the developed epidermis tissue, samples were prepared as described in section 3.1.4. After 6 weeks of culture, the cell-seeded area was cut with a dimension of 1cm×1cm. The electrical resistance of the epidermis model was

directly measured using a multimeter (Fluke 87). 20% cell-free gelatin and gelatin with a confluent cell monolayer were used as control. Samples were prepared in 5 replicates.

### 3.1.7. *In Vitro* Epidermis Drug Permeability

To examine the permeability of the epidermis model, 500 µL of 1 µg/mL of the antibiotic ciprofloxacin (Sigma-Aldrich, USA, Catalog No.: PHR1044-1G) in cell culture media was added onto the seeding zone above the epidermis layer and then the model was incubated at 37 °C. At different time points (0.25, 0.5, 1, 2, and 2.5 h), the media from the channel was transferred into a 96-well plate, and the channel was filled with fresh media. Quantity of diffused ciprofloxacin into the channel was measured using a microplate reader at an excitation wavelength of 270 nm and an emission wavelength of 445 nm. 20% (w/w) cell-free gelatin and gelatin with a confluent cell monolayer were used as control. Samples were prepared in 3 replicates.

Ciprofloxacin standard curve was plotted as fluorescence intensity versus different ciprofloxacin concentrations at 0.03125, 0.0625, 0.125, 0.25, and 0.5 µg/mL (Figure 28). Equation 4 was used to determine the percentage of diffused ciprofloxacin into the samples [73].

$$\text{Diffused ciprofloxacin (\%)} = \frac{Ct \times Vt}{C0 \times V0} \times 100 \quad (4)$$

Where $C_t$ is the ciprofloxacin concentration of samples calculated by a comparison with the standard curves and $V_t$ is the volume of solution removed from the channel at each timepoint. $V_0$ is the total volume of ciprofloxacin solution (500 µL) with the concentration of $C_0$ in the seeding zone (1 µg/mL).

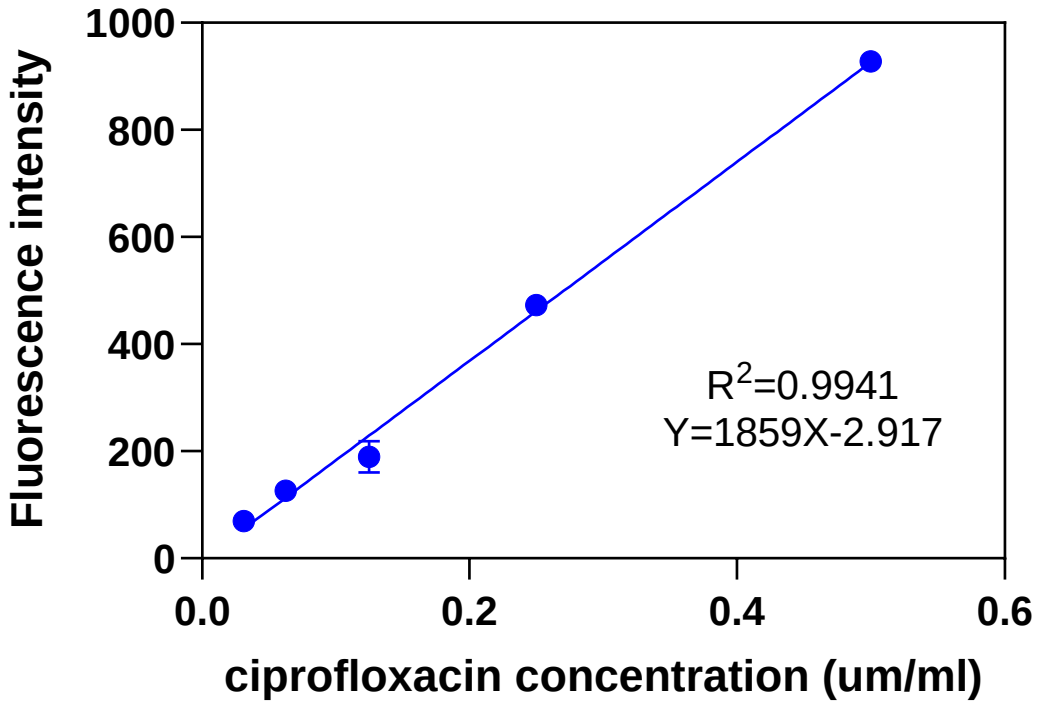


**Figure 28. standard curve correlates the fluorescence intensity to ciprofloxacin concentration. Error bars indicate standard deviation (n=3).**

### 3.1.8. Drug Cytotoxicity Test

To determine the cytotoxicity effects of different concentrations of ciprofloxacin, the HaCaT cells were seeded with a cell density of 50,000 cells/cm2. Ciprofloxacin solutions in cell culture media were prepared with concentrations of 100, 10, 5, 1, 0.5, 0.25, 0.125, 0.0625, and 0.03125. After differentiation, the cells were treated with ciprofloxacin solutions for 3 days. The viability of cells was investigated after 24, 48, and 72 hours post-treatment using PrestoBlue Cell Viability Reagent. Relative viability was calculated by normalizing the fluorescence intensity of each condition with the control condition (no drug).

### 3.1.9. Statistical Analysis

Results were analyzed by GraphPad Prism version 8 (GraphPad Software, La Jolla, CA). Statistical significance was analyzed using one-way ANOVA for more-than-two-group comparisons with one independent variable and two-way ANOVA for more-than-two-group comparisons with two independent variables.

## 3.2. Result and discussion

### 3.2.1. Gelatin Hydrogel Permeability

In order to investigate the permeability of 20% gelatin, the diffusion rate of FITC-Dextran with 70 kD molecular size was studied. The result shows that after 5 hours, more than 50% of FITC-Dextran diffused to a distance of 300 µm from the channel (Figure 29). Considering the distance between the cells on the gel and channel, which is about 200 µm, the permeability of 20% gelatin is adequate for nutrient delivery to the HaCaT cells from the channel.

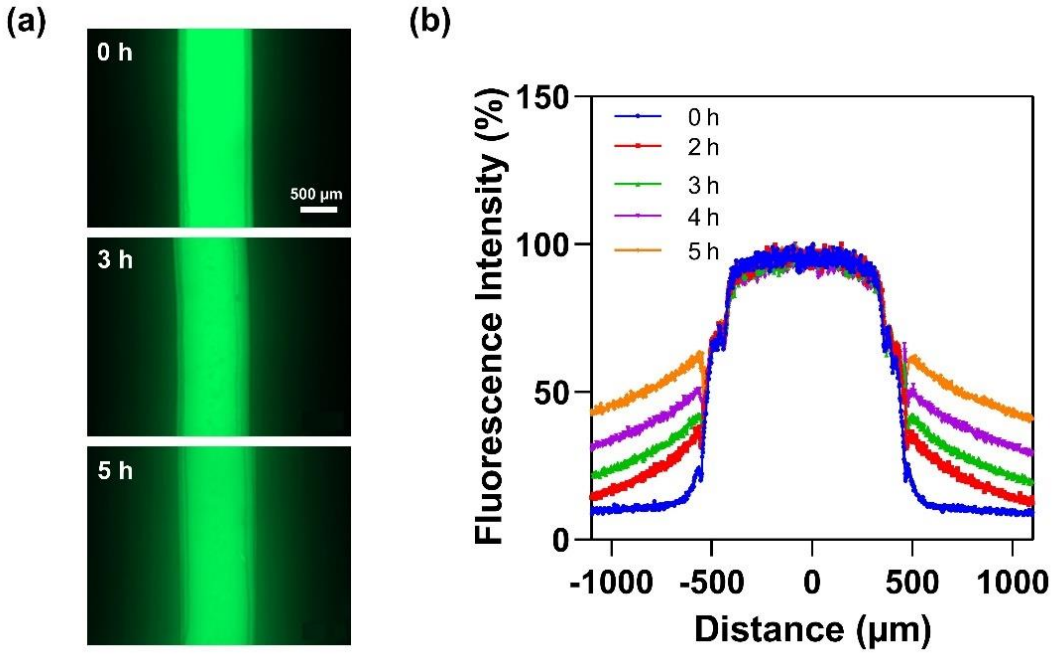


**Figure 29. FITC-Dextran (70 kD) diffusion through the channel to 20% gelatin. Error bars indicate standard deviation (n=3).**

### 3.2.2. Cell Tight Junction Analysis

To evaluate the HaCaT cellscells' tight junction, a confluent monolayer of cells on 20% gelatin was stained with E-cadherin antibody. E-cadherin is not only necessary for cell-cell adhesion, but it affects various cellular functions such as cell signaling and cytoskeleton regulation [83], [84]. The expression of E-cadherin shows that after 7 days of submerged culture, HaCaT cells form a confluent monolayer in which cells have tight junctions (Figure 30).

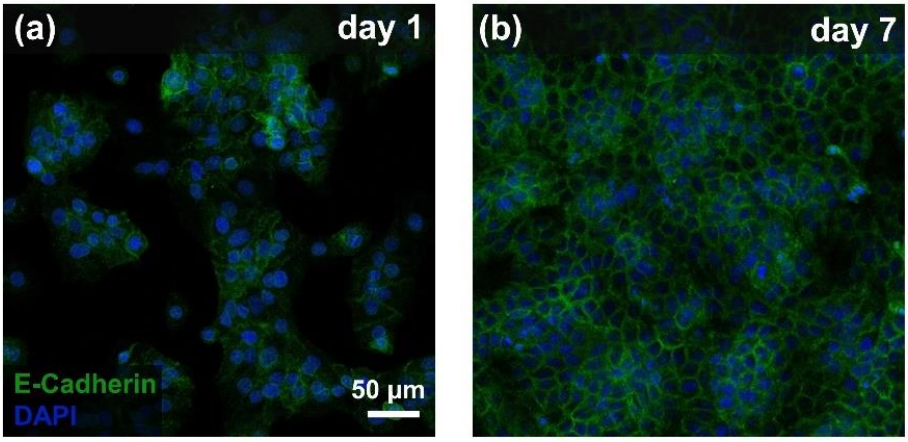


**Figure 30. Fluorescence image of immunocytochemical staining of E-cadherin (green) in HaCaT cell junctions and DAPI for nucleic staining (blue) on day 1 (a) and day 7 (b) when cells reached confluency.**

### 3.2.3. Multilayer Epidermis Formation

After a monolayer of HaCaT cells was formed within 5-7 days of submerged culture, the media was removed from the seeding zone and the differentiation media was delivered to the cells through the channel, maintaining the cells at the air-liquid interface. HaCaT differentiation and stratification started under the air-liquid-interface condition. After 6 weeks of culture at the air-liquid interface, the multilayer structure of keratinocytes formed (Figure 31) and the protein expression of differentiated keratinocytes was studies. Filaggrin as a late epidermal differential marker has a pivotal role in the skin barrier function [85]. To investigate the protein expression of the reconstructed epidermis on 20% gelatin, The Filaggrin antibody was used to confirm the presence of terminally differentiated keratinocytes after 6 weeks of differentiation (Figure 31). The epidermis model exhibited a positive expression of Filaggrin in green (and the nuclei in blue). However, keratinocytes'

structure was slightly disorganized which is possibly due to the immature terminal differentiation of HaCaT cells and the absence of other cell types such as fibroblasts [73].

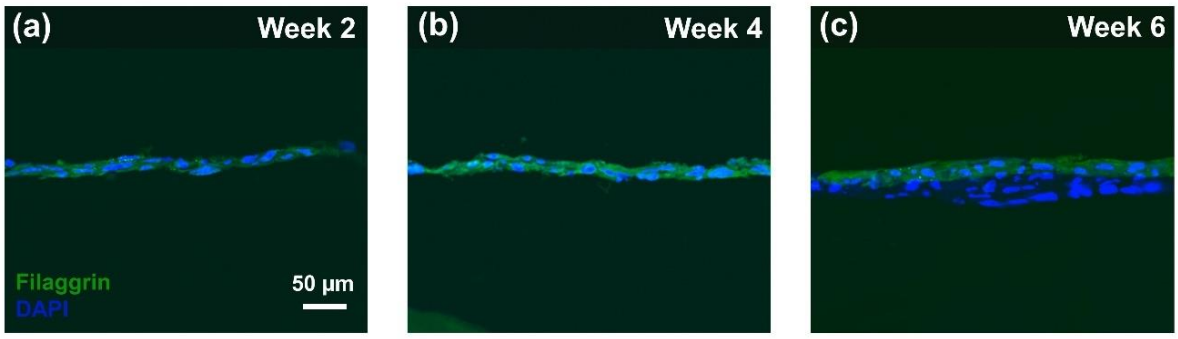


**Figure 31. Fluorescence image of immunocytochemical staining of Filaggrin protein (green, late differentiation marker of HaCaT cells) and nuclei with DAPI (blue) in week 2 (a), 4 (b), and 6 (c)**

### 3.2.4. *In Vitro* Epidermis Barrier Function

To study the barrier function of the *in vitro* epidermis model, the electrical resistance of the epidermis model was measured. The results show that the epidermis model successfully provides a higher electrical resistance with 3.5±0.3 kΩ comparing to the bare gelatin hydrogel with 2.0±0.4 kΩ electrical resistance and 2D cell culture on gelatin with 2.5±0.4 (Figure 32). It is probably due to the functional tight junctions of keratinocytes and the presence of filaggrin protein in the epidermis model. However, the lower degree of stratification in differentiated HaCaTs and the absence of other skin layers resulted in a resistance on the lower end of the range for human skin, which has an electrical resistance of 1-10 kΩ [73].

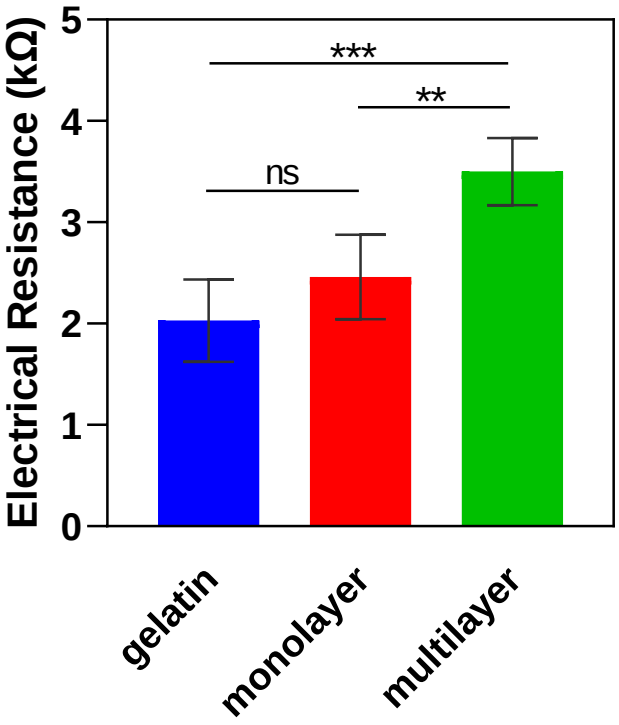


**Figure 32. Electrical resistance of cell-free gelatin, gelatin with 2D monolayer cell, and multilayer structure of the developed epidermis. Error bars indicate standard deviation (n=5, ns, **, and *** indicate nonsignificant, $p<0.01$, and $p<0.001$ respectively)**

In addition to electrical resistance, the drug permeability of the *in vitro* epidermis model was studied by measuring the percentage of penetrated ciprofloxacin from the epidermis surface to the channel. Results show that the epidermis model with 24.4% permeability significantly hinders the drug permeation to the channel when compared to the cell-free gelatins with 42.7% and 2D cell culture on gelatin with 41.3% permeability (Figure 33).

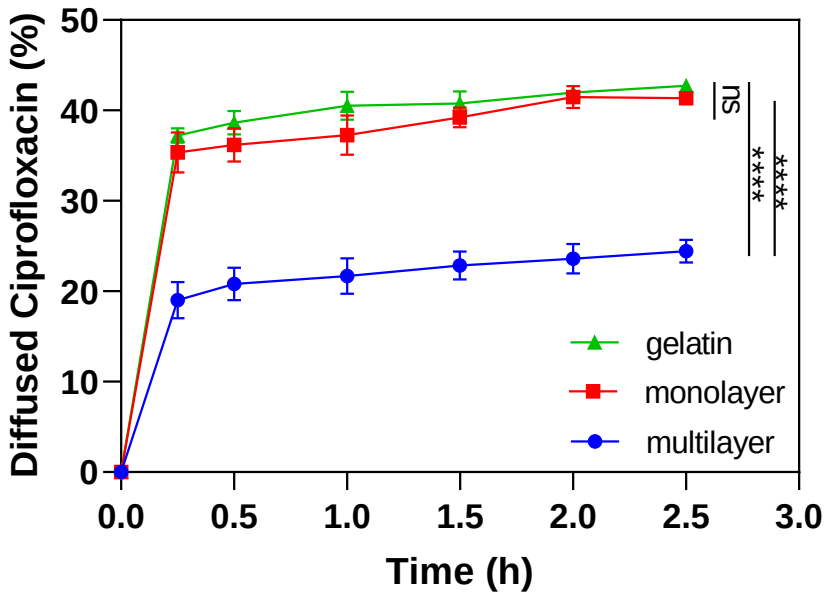


**Figure 33. Ciprofloxacin diffusion from the surface of 20% gelatin to channel indicating the barrier function of epidermis. Error bars indicate standard deviation (n=3, ns, **, and **** indicate nonsignificant, $p<0.01$, and $p<0.0001$ respectively)**

### 3.2.5. Drug Cytotoxicity Test

To study the viability of HaCaT cells treated with various dosages of the drug, cells were treated with different ciprofloxacin concentrations and the viability of HaCaT cells was studied using PrestoBlue cell viability reagent. The percentages of viable cells show that ciprofloxacin with 100 µg/mL concentration can significantly decrease the cell viability after 48 hours of treatment comparing to the control while 10 µg/mL treatment affects the cell viability after 72 hours exposure (Figure 34). This result is consistent with the results of previous studies on fibroblast cell viability with different concentrations of ciprofloxacin [38], [39]. The lower concentration of ciprofloxacin, on the other hand, does not adversely affect the cells viability.

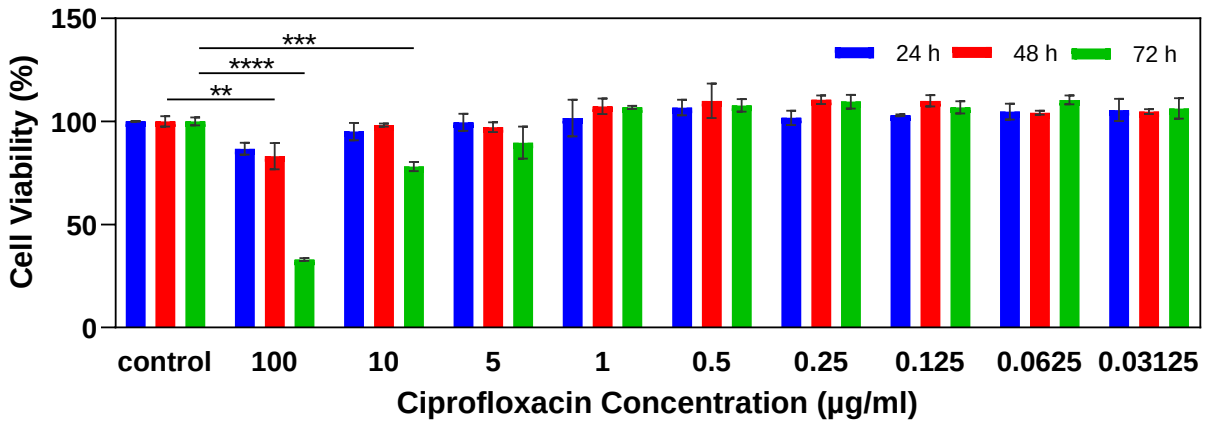


**Figure 34. Cytotoxic effect of different concentrations of ciprofloxacin on HaCaT cells. Error bars indicate standard deviation (n=3, ns, **, ***, and **** indicate nonsignificant, $p<0.01$, $p<0.001$, and $p<0.0001$ respectively)**

## 3.3. Conclusion

The 20% (w/w) gelatin hydrogel and the extrusion-based 3D printer were used to fabricate a suitable scaffold with an embedded channel for developing an epidermis tissue model. The embedded hallow channel mimicked a microvessel in the dermal layer and provide the epidermis tissue at air-liquid interface with substantial nutrients and growth factors. The results of this study showed that HaCaT cells after 6 weeks of culture at air-liquid-interface developed a multilayer structure and expressed late differential markers in the outermost layer. This multilayer structure with the presence of a complex network of intracellular proteins offered a superior barrier functionality in comparison with cell-free gelatin hydrogel and gelatin with a monolayer cell. It demonstrates that this model represents the native epidermis tissue more closely than 2D monolayer cultures.

# Chapter 4: Development of an Infected Wound Model

In addition to the physical barrier, the epidermis actively contributes to the immunologic barrier function by the expression of Toll-like receptors (TLRs) on keratinocytes (Figure 35) [86]. TLRs are pattern recognition receptors (PRRs) which play a central role in host defense mechanisms against pathogenic microorganisms by activating the early innate immune system [86]–[88]. These receptors recognize pathogen-associated molecular patterns (PAMPs) of microorganisms and lead to activation of several intracellular signaling cascades including activation of nuclear factor-κB (NF-κB) [86], [88]. NF-κB is a protein complex that regulates genes involved in immune responses such as expression of cytokines and other inflammatory molecules such as tumor necrosis factor alpha (TNF-α), interleukin 1 beta, 6, and 8 (IL-1β, IL-6, and IL-8) [86], [89]. Inflammatory response serves as a protective activity to restore the homeostatic state after a harmful disturbance. Infections originating from various microorganisms can activate the innate immune system to defend against the invading pathogen by stimulating the expression of proinflammatory cytokines by immune cells such as monocytes and macrophages or keratinocytes [88]. To date, 10 TLRs have been identified and each TLR is responsible for recognizing specific PAMPs (Figure 35) [86], [88]. For instance, TLR5 recognized bacterial flagellin while TLR4 detects liposaccharide (LPS) of Gram-negative bacteria such as *Escherichia coli* (*E. coli*) [86], [89].

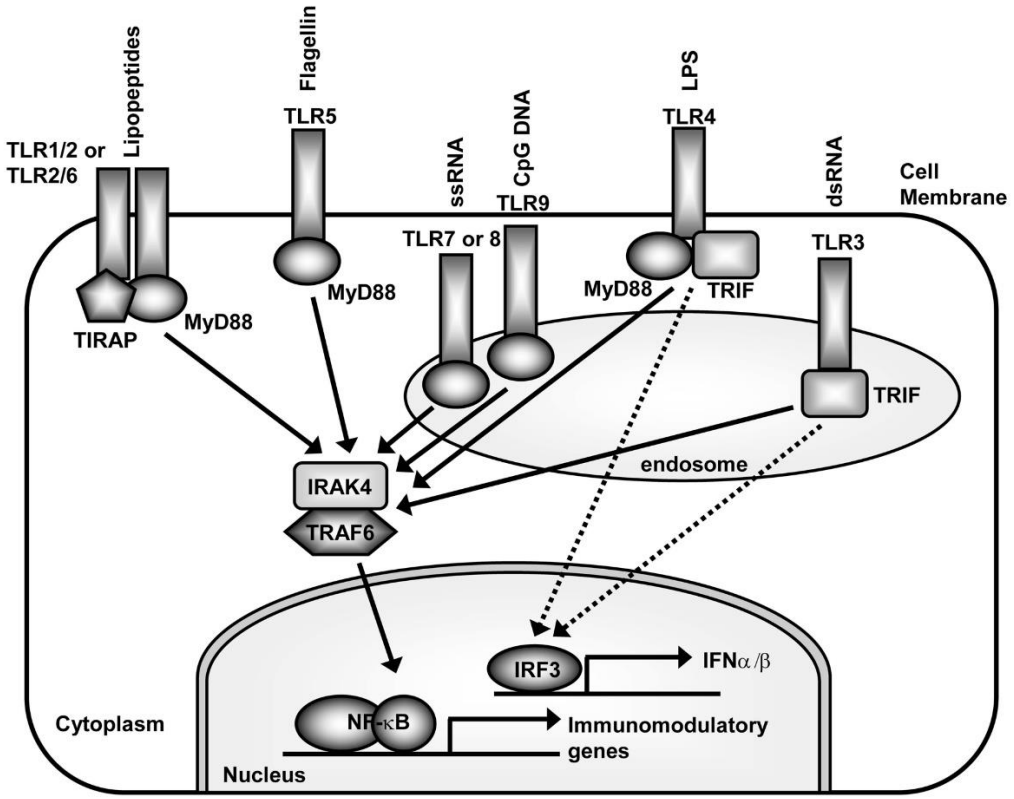


**Figure 35. Pathogen-associated molecular patterns recognized by TLRs, the cellular location of TLRs and the different MyD88 adapters used by TLRs that promote distinct immune responses** [86]**.**

*E. coli* is one of the most abundant bacteria living on human skin and they usually do not cause infection on healthy skin due to the presence of antimicrobial peptides produced by keratinocytes [90]. However, there are several reports that show *E. coli* can cause surgical site infection and post-burn or injury infection [91]. In this chapter, the application of the developed epidermis model in studying the skin proinflammatory response to *E. coli*-induced infection has been investigated. To investigate the proinflammatory response of keratinocytes to *E. coli*, we analyzed the level of expression of IL-1β and TNF-α (Figure 36). IL-1β and TNF-α in turn function through autocrine signaling on keratinocytes and result in the expression of other proinflammatory cytokines such as IL-6 and IL-8 [58].

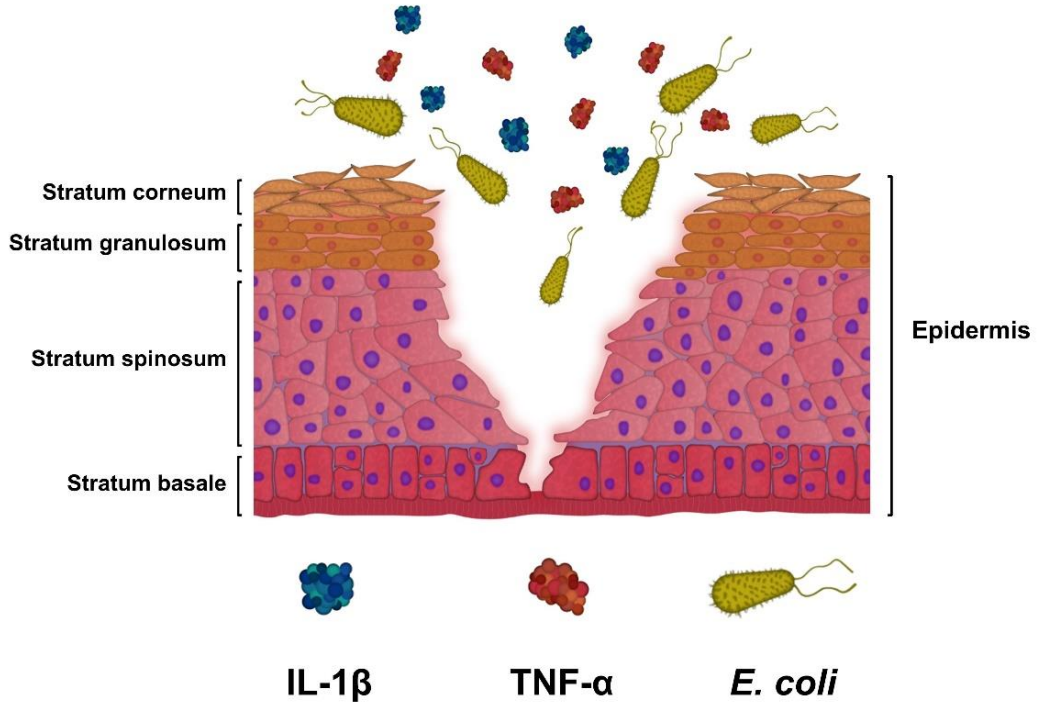


**Figure 36. Schematic picture of an infected wound representing keratinocytes response to *E. coli***

## 4.1. Materials and methods

### 4.1.1. Bacterial Study

HaCaT-seeded gelatins were prepared then the media was removed and substituted with 1 mL of fresh antibiotic-free media two days before infecting with bacteria. A single colony of *E. coli* (W3110, ATCC, USA, Catalog No.: 27325) was inoculated into 10 mL LB broth (Difco™ LB Broth, Lennox, Thermo Fisher Scientific, USA, Catalog No.: DF0402170) culture medium overnight. After being incubated and reaching OD600 of ≈0.4, bacteria solution with the concentration of $10^8$ cells/mL was prepared. Three groups of samples were prepared; i) control group treated with 25 µl/sample bacteria-free PBS, ii) and iii) treated group incubated with 25 µL of bacteria solution. After 2 hours of incubation, the

media of each group were substituted with the fresh media to remove the non-adherent bacteria and 10 µL of ciprofloxacin solution with a concentration of 400 µg/mL was added to the third group.

### 4.1.2. Scratch Wound Healing Assay

To study the healing of infected and treated wound models, samples were prepared as described above and a scratch was created on the epidermis construct using a 200 µl micropipette tip and then infected with *E. coli*. For the purpose of studying the efficacy of treatments on cell migration, samples were imaged at 0, 24, and 48 hours. Images were taken by microscope using bright field and cell migration activity was evaluated by measuring the scratched area using Image J software (NIH, Bethesda, MD, USA). For each sample, three images were taken from randomly selected areas. Experiments were conducted independently in triplicate.

### 4.1.3. Proinflammatory Cytokine Analysis

To study the inflammatory response of the epidermis model to infection, samples were prepared as described above in two sets, one for collecting the supernatant and the second for culturing the swabs from each sample on nutrient agar sheets at 8 and 24 hours for CFU counting. The expression of two proinflammatory cytokines, IL-1β and TNF-α, was measured using Human Mini ABTS ELISA Development Kit (Peprotech, USA, Catalog No.: 900-M95 and 900-M25).

### 4.1.4. Statistical Analysis

Results were analyzed by GraphPad Prism version 8 (GraphPad Software, La Jolla, CA). Statistical significance was analyzed using one-way ANOVA for more-than-two-group

comparisons with one independent variable and two-way ANOVA for more-than-two-group comparisons with two independent variables.

## 4.2. Result and discussion

### 4.2.1. Scratch Wound Healing Assay

To mimic an infected wound *in vitro*, a scratch was created on epidermis construct using a 200 µl micropipette tip and then infected with *E. coli* which is one of the most common gram-negative bacteria (Figure 37 A). Ciprofloxacin as an antimicrobial agent was used to treat the infected model. Three groups were considered for the wound healing study including i) infected model with 0.4 µg/mL ciprofloxacin treatment, ii) infected model without treatment, and iii) uninfected model without ciprofloxacin as control. Scratch closure was monitored using bright-field images of the samples taken after 24 and 48 hours. Results show that scratch in the control and treated groups were closed with a similar behavior while the scratch in the untreated infected model remained unchanged (Figure 37 A and B). This result implies that *E. coli* can interfere with cell proliferation or migration to the injured site.

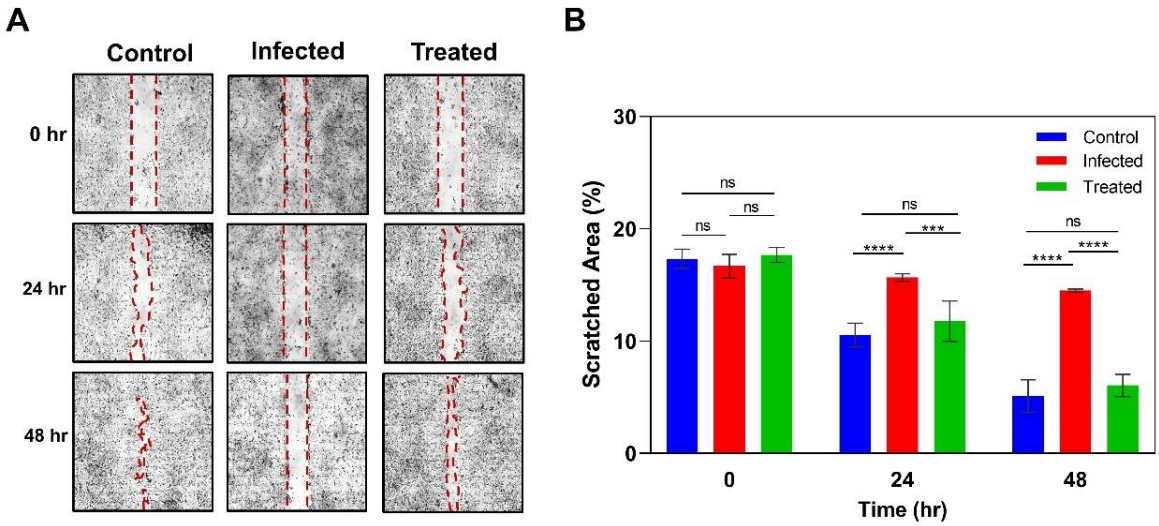


**Figure 37. A) Scratch assay on control, infected sample with *E. coli*, and infected sample with *E. coli* and treated with ciprofloxacin, B) the percentage of scratched area using NIH ImageJ. Error bars indicate standard deviation (n=3, ns, ***, and **** indicate nonsignificant, $p<0.001$, and $p<0.0001$ respectively)**

### 4.2.2. Colony Forming Unit Counting

To investigate the effectiveness of ciprofloxacin treatment, swabs were taken from samples after 8 and 24 hours and cultured on nutrient agar sheets. The results of colony-forming units (CFU) counting as an indicator of the number of bacteria showed that after 8 hours there were about 600 CFU/cm$^2$ in the infected model which grew to about 1000 CFU/cm$^2$ in 24 hours (Figure 38). Meanwhile, in the control and treated samples, no significant bacteria colonies were observed. This confirmed that ciprofloxacin was effective for treating infections from *E. coli*.

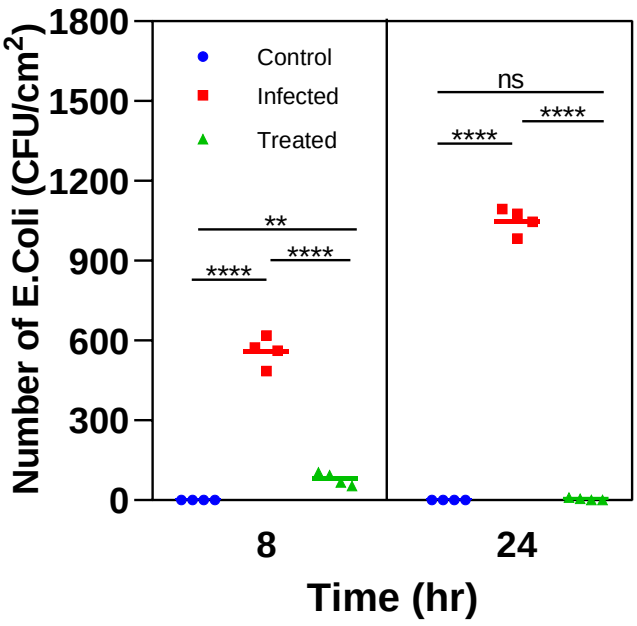


**Figure 38. *E. coli* CFU numbers per unit cell cultured area after 8 and 24-hour bacteria induction (n=3, ns, **, and **** indicate nonsignificant, $p<0.01$, and $p<0.0001$ respectively).**

### 4.2.3. Proinflammatory Response

To investigate the proinflammatory response of keratinocytes to infection, we analyzed the TNF-α and IL-1β expression in HaCaT cells challenged with *E. coli* The results show that after 8 hours exposure to *E. coli* HaCaT cells in infected samples produced significantly higher levels of IL-1β (1311±90 pg/mL) and TNF-α (1977±262 pg/mL) with respect to the control group (383±80 pg/mL IL-1β and 949±215 pg/mL TNF-α) which was further increased after 24 hours of exposure to *E. coli* (Figure 39 A and B). Treatment with 4 µg/mL ciprofloxacin reduced the level of IL-1β and TNF-α in the infected samples to 795 and 1417 pg/mL respectively. However, the level of IL-1β and TNF-α were still significantly higher than the control group. After 24 hours of treatment, however, the level of TNF-α and IL-1β decreased to 246 and 1142 pg/mL respectively and with insignificant

difference reached the same level as the control group. The trend of inflammatory cytokines expression is consistent with CFU counting results and confirms the effectiveness of the drug in treating *E. coli* infection and terminating the inflammatory response of keratinocytes.

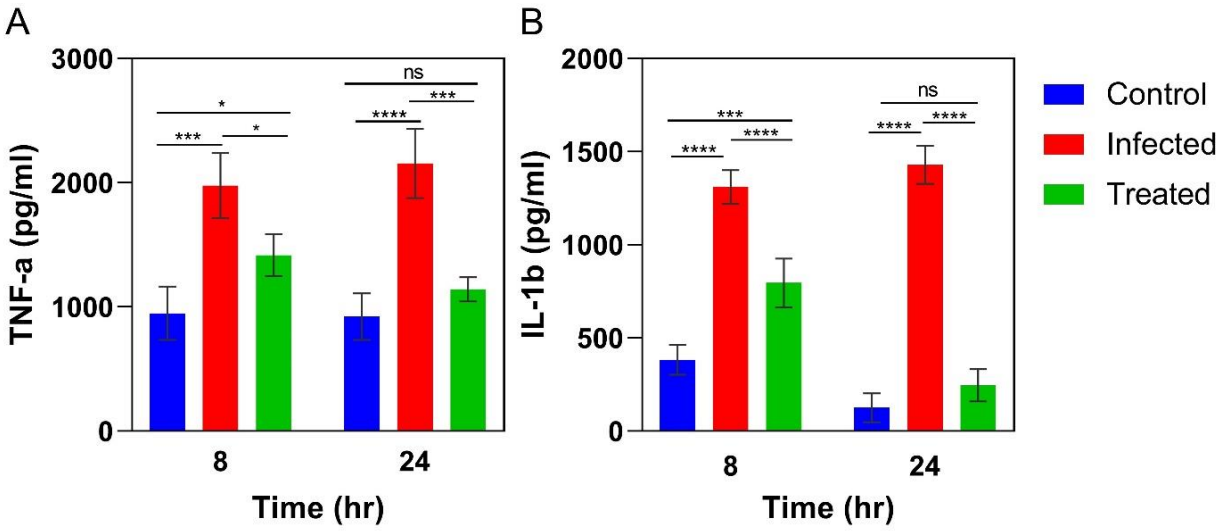


**Figure 39. A) expression of TNF-α by HaCaT cells in response to *E. coli* in control, infected, and ciprofloxacin-treated samples, B) expression of IL-1β by HaCaT cells in response to infection in control, infected, and ciprofloxacin-treated samples. Error bars indicate standard deviation (n=3, ns, *, ***, and **** indicate nonsignificant, $p<0.1$, $p<0.001$, and $p<0.0001$ respectively)**

## 4.3. Conclusion

Epidermis plays a critical role in protecting the human body from external chemical agents, mechanical forces, and radiation. In addition, it is actively involved in initiating the host's innate immune system by expression of pattern recognition receptors, antimicrobial peptides, chemokines, and proinflammatory cytokines. Studying the proinflammatory response of the skin and the healing mechanism of wounds can help researchers to discover or optimize the therapeutic agents as well as developing more advanced drug delivery

systems. In this chapter, the simplified developed epidermis model was used to study the healing time of infected and non-infected wounds and the production of two main proinflammatory cytokines in response to infection. For this purpose, the levels of TNF-α and IL-1β were studied. The results showed that the level of both TNF-α and IL-1β increased over time in infected samples while treatment with ciprofloxacin caused a drastic reduction in the level of them in treated samples. Finally, after 24 hours of treatment with ciprofloxacin the level of TNF-α and IL-1β in treated samples were reduced to the same level as control.

# Conclusion and Future Direction

The skin as our outermost organ is always in contact with environmental chemicals, mechanical forces, radiation, and microorganisms. The healthy skin serves as a barrier and protects the human body from external threats such as harmful chemicals and pathogens. However, wounds and injuries depending on the degree of chronicity can interfere with human skin function and cause more serious diseases. The increasing number of patients suffering from chronic wounds and the high cost of their treatment have become a huge worldwide burden. Moreover, the lack of a deep understanding of wound healing mechanisms as well as inefficient drug delivery systems have resulted in the failure of wound treatment approaches. Thus, there are many ongoing projects on modeling the different types of wounds to understand the healing mechanism, wound healing impediments, and optimizing the therapeutic agents and drug delivery systems.

Currently, skin wound modeling mainly relies on animal models including mice, rats, rabbits, and pigs. However, animal models are associated with several problems including inter-species discrepancies and ethical and regulatory issues. To resolve the physiological differences between animal models and human skin, using *ex vivo* human skin obtained from surgical processes has been introduced. However, conducting high throughput studies is challenging due to the short life span of tissues after excision and the limited number of donors. The emergence of *in vitro* models evolving out of 2D cell cultures has provided new avenues toward developing more complex skin models accurately mimicking the *in vivo* physiological environment of human skin. To date, there are several successful *in vitro* healthy skin models. These models are developed by applying tissue engineering, microfluidics, and 3D bioprinting techniques and validated by different analytical

techniques. However, the application of these models in skin wound modeling and studying the healing mechanism has not been confirmed yet.

In this study, we developed a simplified functional *in vitro* skin model using enzymatically crosslinked gelatin with a vasculature channel embedded in the gelatin for nutrient delivery. The epidermis construct was used for infected wound modeling and studying the proinflammatory response. The effects of gelatin and transglutaminase concentrations were studied on the mechanical properties of gelatin hydrogel and the subsequent cell attachment and proliferation. Results showed that the higher gelatin concentration strongly supported cell attachment and proliferation and showed significantly prolonged degradation compared to the lower concentrations. Therefore, the higher concentration of gelatin (20% w/w) was selected for the model development. HaCaT cells were cultured on the fabricated hydrogel model for 7 days submerged in culture media, followed by additional an 6 weeks of culture at the air-liquid interface. The results showed that HaCaT cells terminally differentiated and formed the multilayer structure of the epidermis. The developed epidermis model showed the barrier functions in terms of electrical resistance and drug permeability. Although this epidermis model lacked complete stratification and cell organization due to the absence of fibroblast cells in the construct, it is still a functional *in vitro* construct for wound modeling and drug testing. The *in vitro* epidermis model was used for studying the proinflammatory response of HaCaT cells to infection, and the effectiveness of ciprofloxacin, in infection treatment. The developed epidermis model has great potential for large-scale infected wound modeling, studying drug cytotoxicity, and developing trans-epidermal drug delivery systems because of its functionality, low fabrication cost, and reproducibility.

For the future, there are more differentiation and proliferation markers including K10, K19, and Ki67 to be studied with quantitative polymerase chain reaction (qPCR) machine and immunostaining. Moreover, to improve the complexity of the developed model, other skin cell types such as human dermal fibroblasts and adipocytes (fat cells) can be incorporated into the gelatin hydrogel to provide the dermis and hypodermis layer respectively. In addition, to make the embedded channel more functional, human endothelial cells can be seeded into the interior surface of the channel to form endothelium. Then the differentiation of endothelial cells and lumen formation can be validated by immunostaining the platelet endothelial cell adhesion molecule also known as CD31.

# Bibliography

[1] V. Planz, C. Lehr, and M. Windbergs, “In vitro models for evaluating safety and ef fi cacy of novel technologies for skin drug delivery,” *J. Control. Release*, vol. 242, pp. 89–104, 2016.

[2] W. L. Ng, W. Y. Yeong, and M. W. Naing, “Cellular Approaches to Tissue-Engineering of Skin : A Review,” *J. tissue Sci. Eng.*, vol. 6, no. 2, pp. 150–162, 2015.

[3] J. A. McGrath and J. Uitto, *Anatomy and Organization of Human Skin*, vol. 1. 2010.

[4] S. H. Mathes, H. Ruffner, and U. Graf-hausner, “The use of skin models in drug development,” *Adv. Drug Deliv. Rev.*, vol. 69–70, pp. 81–102, 2014.

[5] A. Isriany Ismail, Surya Ningsi, Nurshalati Tahar, “Anatomy and Physiology of the Skin,” *Jf Fik Uinam*, vol. 2, no. 2, p. 120, 2014.

[6] K. Kabashima, T. Honda, F. Ginhoux, and G. Egawa, “The immunological anatomy of the skin,” *Nat. Rev. Immunol.*, vol. 19, no. 1, pp. 19–30, 2019.

[7] J. A. Hodge, T. A. Rohrer, M. J. Van Beek, D. J. Margolis, A. J. Sober, and M. A. Weinstock, “The burden of skin disease in the United States,” *J. Am. Dermatology*, vol. 76, no. 5, pp. 958–972, 2017.

[8] M. T. L. Chandan K. Sen, Gayle M. Gordillo, Sashwati Roy, Robert Kirsner, Lynn Lambert, Thomas K. Hunt, Finn Gottrup, Geoffrey C. Gurtner, “Human skin wounds: A major and snowballing threat to public health and the economy,” *Wound Repair Regen.*, vol. 17, no. 6, pp. 763–771, 2009.

[9] I. H. Tatiana Demidova-Rice, Michael Hamblin, “Acute and Impaired Wound Healing: Pathophysiology and Current Methods for Drug Delivery, Part 1: Normal

and Chronic Wounds: Biology, Causes, and Approaches to Care," *Adv. Ski. wound care*, vol. 25, no. 7, pp. 304–314, 2013.

[10] T. Velnar, T. Bailey, and V. Smrkolj, "The wound healing process: An overview of the cellular and molecular mechanisms," *J. Int. Med. Res.*, vol. 37, no. 5, pp. 1528–1542, 2009.

[11] W. K. Stadelmann, A. G. Digenis, and G. R. Tobin, "Impediments to wound healing," *Am. J. Surg.*, vol. 176, no. 2, pp. 39–47, 1998.

[12] M. S. Bader, "Diabetic foot infection," *Am. Fam. Physician*, vol. 78, no. 1, pp. 71–79, 2008.

[13] G. A. James *et al.*, "Biofilms in chronic wounds," *Wound Repair Regen.*, vol. 16, no. 1, pp. 37–44, 2008.

[14] J. M. Martin, J. M. Zenilman, and G. S. Lazarus, "Molecular microbiology: New dimensions for cutaneous biology and wound healing," *J. Invest. Dermatol.*, vol. 130, no. 1, pp. 38–48, 2010.

[15] G. Maboni *et al.*, "A novel 3D skin explant model to study anaerobic bacterial infection," *Front. Cell. Infect. Microbiol.*, vol. 7, no. 404, pp. 1–12, 2017.

[16] N. Gøril Eide Flaten, Zora Palac, André Engesland, Jelena Filipovic´-Grcˇic´, Zˇeljka Vanic´, Škalko-Basnet, "In vitro skin models as a tool in optimization of drug formulation," *Eur. J. Pharm. Sci.*, vol. 75, pp. 10–24, 2015.

[17] E. Kugelberg, T. Norstro, T. K. Petersen, T. Duvold, D. I. Andersson, and D. Hughes, "Establishment of a Superficial Skin Infection Model in Mice by Using Staphylococcus aureus and Streptococcus pyogenes," *Antimicrob. Agents Chemother.*, vol. 49, no. 8, pp. 3435–3441, 2005.

[18] A. Aijaz and R. Faulknor, “Hydrogel Microencapsulated Insulin-Secreting Cells Increase Keratinocyte Migration, Epidermal Thickness, Collagen Fiber Density, and Wound Closure in a Diabetic Mouse Model of Wound Healing,” *Tissue Eng. - Part A*, vol. 1, no. 21, pp. 2723–2732, 2015.

[19] N. Malachowa, S. D. Kobayashi, K. R. Braughton, and F. R. Deleo, *Mouse Model of Staphylococcus aureus Skin Infection*, no. 1031. 2013.

[20] L. Mo and A. Tarkowski, “An Experimental Model of Cutaneous Infection Induced by Superantigen-Producing Staphylococcus aureus,” *J. Investig. dematology*, vol. 114, no. 6, pp. 1120–1125, 2000.

[21] S. A. Horst *et al.*, “A Novel Mouse Model of Staphylococcus aureus Chronic Osteomyelitis That Closely Mimics the Human Infection An Integrated View of Disease Pathogenesis,” *AJPA*, vol. 181, no. 4, pp. 1206–1214, 2012.

[22] N. Nippe *et al.*, “Subcutaneous Infection with S . aureus in Mice Reveals Association of Resistance with Influx of Neutrophils and Th2 Response,” *J. Investig. dematology*, vol. 131, no. 6, pp. 125–132, 2011.

[23] C. Schaudinn, C. Dittmann, J. Jurisch, and M. Laue, “Development , standardization and testing of a bacterial wound infection model based on ex vivo human skin,” *PLoS One*, vol. 12, no. 11, pp. 1–13, 2017.

[24] G. Maboni *et al.*, “A Novel 3D Skin Explant Model to Study Anaerobic Bacterial Infection,” *Front. Cell. Infect. Microbiol.*, vol. 7, pp. 1–12, 2017.

[25] T. A. Andrade *et al.*, “Ex vivo model of human skin (hOSEC) as alternative to animal use for cosmetic tests,” *Procedia Eng.*, vol. 110, no. 16, pp. 67–73, 2015.

[26] D. E. Corzo-León, C. A. Munro, and D. M. MacCallum, “An ex vivo human skin

model to study superficial fungal infections," *Front. Microbiol.*, vol. 10, no. 1172, pp. 1–17, 2019.

[27] N. T. D. A. Peres *et al.*, "In vitro and ex vivo infection models help assess the molecular aspects of the interaction of Trichophyton rubrum with the host milieu," *Med. Mycol.*, vol. 54, no. 4, pp. 420–427, 2016.

[28] M. O. Danso, T. Berkers, A. Mieremet, F. Hausil, and J. A. Bouwstra, "An ex vivo human skin model for studying skin barrier repair," *Exp. Dermatol.*, vol. 24, no. 1, pp. 48–54, 2015.

[29] E. A. Khalil, M. Y. Alkawareek, G. Othman, B. Tbakhi, and A. G. Al-Bakri, "Evaluation of paromomycin sulphate permeation using ex vivo human skin model," *Pharm. Dev. Technol.*, vol. 24, no. 3, pp. 390–393, 2019.

[30] A. S. Bu *et al.*, "S100A15 , an Antimicrobial Protein of the Skin : Regulation by E . coli through Toll-Like Receptor 4," *J. Investig. dematology*, vol. 127, no. 11, pp. 2596–2604, 2007.

[31] S. Gupta, C. Tang, M. Tran, and D. E. Kadouri, "Effect of Predatory Bacteria on Human Cell," *PLoS One*, vol. 11, no. 8, pp. 1–15, 2016.

[32] A. A. Chaudhari *et al.*, "A three-dimensional human skin model to evaluate the inhibition of Staphylococcus aureus by antimicrobial peptide-functionalized silver carbon nanotubes," *J. Biomater. Appl.*, vol. 33, no. 7, pp. 924–934, 2019.

[33] S. E. L. Vidal, K. A. Tamamoto, H. Nguyen, R. D. Abbott, D. M. Cairns, and D. L. Kaplan, "3D biomaterial matrix to support long term, full thickness, immuno-competent human skin equivalents with nervous system components," *Biomaterials*, vol. 198, pp. 194–203, 2019.

[34] A. Mieremet, M. Rietveld, R. Van Dijk, J. A. Bouwstra, and A. El Ghalbzouri, “Recapitulation of Native Dermal Tissue in a Full-Thickness Human Skin Model Using Human Collagens,” *Tissue Eng. - Part A*, vol. 24, no. 11–12, pp. 873–881, 2018.

[35] A. Abtin *et al.*, “Escherichia coli ghosts promote innate immune responses in human keratinocytes,” *Biochem. Biophys. Res. Commun.*, vol. 400, no. 1, pp. 78–82, 2010.

[36] I. Colombo *et al.*, “HaCaT Cells as a Reliable In Vitro Differentiation Model to Dissect the Inflammatory / Repair Response of Human Keratinocytes,” *Mediators Inflamm.*, vol. 2017, pp. 11–22, 2017.

[37] T. Magcwebeba, S. Riedel, S. Swanevelder, P. Bouic, P. Swart, and W. Gelderblom, “Interleukin-1 α Induction in Human Keratinocytes ( HaCaT ): An In Vitro Model for Chemoprevention in Skin,” *J. Skin Cancer*, vol. 2012, 2012.

[38] A. F. and F. H. A GuÈrbay, C Garrel, M Osman, M-J Richard, “Cytotoxicity in ciprofloxacin-treated human fibroblast cells and protection,” *Hum. Exp. toxiology*, vol. 21, no. 12, pp. 635–641, 2002.

[39] M. B. Ferreira, S. Myiagi, C. G. Nogales, and M. S. Campos, “Time- and concentration-dependent cytotoxicity of antibiotics used in endodontic therapy,” *J. Appl. oral sicence*, vol. 18, no. 3, pp. 259–263, 2010.

[40] S. Transformed, K. Cell, L. Hacat, E. Boelsma, M. C. H. Verhoeven, and M. Ponec, “Reconstruction of a Human Skin Equivalent Using a,” *J. Invest. Dermatol.*, vol. 112, no. 4, pp. 489–498, 1999.

[41] A. De Breij, E. M. Haisma, M. Rietveld, A. El Ghalbzouri, L. Dijkshoorn, and P. H. Nibbering, “Three-Dimensional Human Skin Equivalent as a Tool To Study

Acinetobacter baumannii Colonization," *Antimicrob. Agents Chemother.*, pp. 2459–2464, 2012.

[42] M. Roger *et al.*, "Bioengineering the microanatomy of human skin," *J. Anat.*, vol. 234, no. 4, pp. 438–455, 2019.

[43] S. Breslin and L. O'Driscoll, "Three-dimensional cell culture: The missing link in drug discovery," *Drug Discov. Today*, vol. 18, no. 5–6, pp. 240–249, 2013.

[44] W. C. Pinar Avci, Magesh Sadasivam, Asheesh Gupta, and M. De Melo, Ying-Ying Huang, Rui Yin, Chandran Rakkiyappan, Raj Kumar, Ayodeji Otufowora, Theodore Nyame, and R. Hamblin, "Animal models of skin disease for drug discovery," *Bone*, vol. 23, no. 1, pp. 1–7, 2008.

[45] X. Ma *et al.*, *Sourcebook of Models For Biomedical Research*, vol. 54, no. 97. 2018.

[46] E. Middelkoop, A. J. Van Den Bogaerdt, E. N. Lamme, M. J. Hoekstra, K. Brandsma, and M. M. W. Ulrich, "Porcine wound models for skin substitution and burn treatment," *Biomaterials*, vol. 25, no. 9, pp. 1559–1567, 2004.

[47] E. Kugelberg, T. Norström, T. K. Petersen, T. Duvold, D. I. Andersson, and D. Hughes, "Establishment of a superficial skin infection model in mice by using Staphylococcus aureus and Streptococcus pyogenes," *Antimicrob. Agents Chemother.*, vol. 49, no. 8, pp. 3435–3441, 2005.

[48] J. M. Davidson, "Animal models for wound repair," *Arch. Dermatol. Res.*, vol. 290, no. 1, pp. 1–11, 1998.

[49] T. Dai, G. B. Kharkwal, M. Tanaka, Y. Y. Huang, V. J. Bil de Arce, and M. R. Hamblin, "Animal models of external traumatic wound infections," *Virulence*, vol. 2, no. 4, 2011.

[50] W. A. Dorsett-Martin and A. B. Wysocki, “Rat models of skin wound healing,” *Source B. Model. Biomed. Res.*, pp. 631–638, 2008.

[51] N. Shanks, R. Greek, and J. Greek, “Are animal models predictive for humans?,” *Philos. Ethics, Humanit. Med.*, vol. 4, no. 1, pp. 1–20, 2009.

[52] J. Bailey and M. Balls, “Recent efforts to elucidate the scientific validity of animal-based drug tests by the pharmaceutical industry, pro-testing lobby groups, and animal welfare organisations,” *BMC Med. Ethics*, vol. 20, no. 1, pp. 1–7, 2019.

[53] M. Wufuer *et al.*, “Skin-on-a-chip model simulating inflammation , edema and drug-based treatment,” *Nat. Publ. Gr.*, vol. 6, pp. 1–12, 2016.

[54] B. P. Ch, “A Review on Drug Testing in Animals,” pp. 1–4, 2016.

[55] D. J. Yoon *et al.*, “A tractable, simplified ex vivo human skin model of wound infection,” *Wound Repair Regen.*, vol. 27, no. 4, pp. 421–425, 2019.

[56] Yanfen Li and Kristopher A. Kilian, “Bridging the gap: from 2D cell culture to 3D microengineered extracellular matrices,” *Physiol. Behav.*, vol. 176, no. 5, pp. 139–148, 2017.

[57] M. J. Randall, A. Jüngel, M. Rimann, and K. Wuertz-Kozak, “Advances in the biofabrication of 3D skin in vitro: Healthy and pathological models,” *Front. Bioeng. Biotechnol.*, vol. 6, p. 154, 2018.

[58] A. Marcatili, G. C. D. I. Ero, M. Galdiero, A. Folgore, and G. Petrillo, “TNF-a, IL-la , IL-6 and lCAM-l expression in human keratinocytes stimulated in vitro with Escherichia coli heat-shock proteins,” *microbiology*, vol. 143, pp. 45–53, 1997.

[59] T. Sun, S. Jackson, J. W. Haycock, and S. MacNeil, “Culture of skin cells in 3D rather than 2D improves their ability to survive exposure to cytotoxic agents,” *J.*

*Biotechnol.*, vol. 122, no. 3, pp. 372–381, 2006.

[60] A. Astashkina, B. Mann, and D. W. Grainger, “A critical evaluation of in vitro cell culture models for high-throughput drug screening and toxicity,” *Pharmacol. Ther.*, vol. 134, no. 1, pp. 82–106, 2012.

[61] G. Sriram *et al.*, “Full-thickness human skin-on-chip with enhanced epidermal morphogenesis and barrier function,” *Mater. Today*, vol. 21, no. 4, pp. 326–340, 2018.

[62] N. Jusoh, J. Ko, and N. L. Jeon, “ Microfluidics-based skin irritation test using in vitro 3D angiogenesis platform ,” *APL Bioeng.*, vol. 3, no. 3, p. 036101, 2019.

[63] B. S. Kim, G. Gao, J. Y. Kim, and D.-W. Cho, “3D Cell Printing of Perfusable Vascularized Human Skin Equivalent Composed of Epidermis, Dermis, and Hypodermis for Better Structural Recapitulation of Native Skin,” *Adv. Healthc. Mater.*, p. 1801019, Oct. 2018.

[64] H. E. Abaci *et al.*, “Human Skin Constructs with Spatially Controlled Vasculature Using Primary and iPSC-Derived Endothelial Cells,” *Adv. Healthc. Mater.*, vol. 5, pp. 1800–1807, 2016.

[65] P. Admane *et al.*, “Direct 3D bioprinted full-thickness skin constructs recapitulate regulatory signaling pathways and physiology of human skin,” *Bioprinting*, vol. 15, p. 51, 2019.

[66] G. Tjabringa and M. Bergers, “Development and Validation of Human Psoriatic Skin Equivalents,” *Am. J. Pathol.*, vol. 173, no. 3, pp. 815–823, 2008.

[67] N. Mori, Y. Morimoto, and S. Takeuchi, “Skin integrated with perfusable vascular channels on a chip,” *Biomaterials*, vol. 116, pp. 48–56, 2017.

[68] F. Groeber, L. Engelhardt, J. Lange, S. Kurdyn, and F. F. Schmid, “A First Vascularized Skin Equivalent as an Alternative to Animal Experimentation,” *ALTEX*, vol. 33, no. 4, pp. 415–422, 2016.

[69] M. Bataillon *et al.*, “Characterization of a new reconstructed full thickness skin model, t-skin™, and its application for investigations of anti-aging compounds,” *Int. J. Mol. Sci.*, vol. 20, no. 9, p. 2240, 2019.

[70] Y. Liu *et al.*, “Validation of a predictive method for sunscreen formula evaluation using gene expression analysis in a Chinese reconstructed full-thickness skin model,” *Int. J. Cosmet. Sci.*, pp. 147–155, 2019.

[71] M. Sheikholeslam, M. E. E. Wright, M. G. Jeschke, and S. Amini-nik, “Biomaterials for Skin Substitutes,” *Adv. Healthc. Mater.*, vol. 7, no. 5, pp. 1–20, 2017.

[72] M. Shimoda, *Tissue Engineering for Artificial Organs*. 2017.

[73] X. Zhao *et al.*, “Photocrosslinkable Gelatin Hydrogel for Epidermal Tissue Engineering,” *Adv. Healthc. Mater.*, vol. 5, no. 1, pp. 108–118, 2016.

[74] J. W. Nichol, S. T. Koshy, H. Bae, C. M. Hwang, S. Yamanlar, and A. Khademhosseini, “Cell-laden microengineered gelatin methacrylate hydrogels,” *Biomaterials*, vol. 31, no. 21, pp. 5536–5544, 2010.

[75] G. Yang, Z. Xiao, X. Ren, H. Long, and H. Qian, “Enzymatically crosslinked gelatin hydrogel promotes the proliferation of adipose tissue-derived stromal cells,” *PeerJ*, vol. 2, pp. 1–22, 2016.

[76] A. L. Paguirigan and D. J. Beebe, “Protocol for the fabrication of enzymatically crosslinked gelatin microchannels for microfluidic cell culture,” *Nat. Protoc.*, vol. 2, pp. 1782–1788, 2007.

[77] C. Ceccaldi *et al.*, “Validation and application of a nondestructive and contactless method for rheological evaluation of biomaterials,” *J. Biomed. Mater. Res. - Part B Appl. Biomater.*, vol. 105, no. 8, pp. 2565–2573, 2017.

[78] O. Chaudhuri, “Viscoelastic hydrogels for 3D cell culture,” *Biomater. Sci.*, vol. 5, no. 8, pp. 1480–1490, 2017.

[79] O. Coculture, V. M. Schoop, N. Mirancea, and N. E. Fusenig, “Epidermal Organization and Differentiation of HaCaT,” *J. Invest. Dermatol.*, vol. 112, no. 3, pp. 343–353, 1999.

[80] S. V. Murphy and A. Atala, “3D bioprinting of tissues and organs,” *Nat. Biotechnol.*, vol. 32, no. 8, pp. 773–785, 2014.

[81] C. Mandrycky, Z. Wang, K. Kim, and D. H. Kim, “3D bioprinting for engineering complex tissues,” *Biotechnol. Adv.*, vol. 34, no. 4, pp. 422–434, 2016.

[82] R. Suntornnond, E. Yong, S. Tan, J. An, and C. K. Chua, “A highly printable and biocompatible hydrogel composite for direct printing of soft and perfusable vasculature-like structures,” *Sci. Rep.*, no. June, pp. 1–11, 2017.

[83] J. A. Tunggal *et al.*, “E-cadherin is essential for in vivo epidermal barrier function by regulating tight junctions,” *EMBO J.*, vol. 24, no. 6, pp. 1146–1156, 2005.

[84] M. F. Izaguirre *et al.*, “Role of E-cadherin in epithelial architecture maintenance,” *Cell Commun. Adhes.*, vol. 17, no. 1, pp. 1–12, 2010.

[85] A. Sandilands, C. Sutherland, A. D. Irvine, and W. H. I. Mclean, “Filaggrin in the frontline : role in skin barrier function and disease,” *J. Cell Sci.*, vol. 122, pp. 1285–1294, 2009.

[86] L. S. Miller, “Toll-Like Receptors in Skin,” *Adv. Dermatol.*, vol. 24, no. C, pp. 71–

87, 2008.

[87] S. Krishna and L. S. Miller, “Host – pathogen interactions between the skin and Staphylococcus aureus,” *Curr. Opin. Microbiol.*, vol. 15, no. 1, pp. 28–35, 2012.

[88] L. Feldmeyer, S. Werner, L. E. French, and H. Beer, “Interleukin-1 , inflammasomes and the skin,” *Eur. J. Cell Biol.*, vol. 89, no. 9, pp. 638–644, 2010.

[89] R. I. Tapping, S. Akashi, K. Miyake, P. J. Godowski, and P. S. Tobias, “ Toll-Like Receptor 4, But Not Toll-Like Receptor 2, Is a Signaling Receptor for Escherichia and Salmonella Lipopolysaccharides ,” *J. Immunol.*, vol. 165, no. 10, pp. 5780–5787, 2000.

[90] R. Gläser, J. Harder, H. Lange, J. Bartels, E. Christophers, and J. M. Schröder, “Antimicrobial psoriasin (S100A7) protects human skin from Escherichia coli infection,” *Nat. Immunol.*, vol. 6, no. 1, pp. 57–64, 2005.

[91] Ž. Petkovšek, K. Eleršič, M. Gubina, D. Žgur-Bertok, and M. S. Erjavec, “Virulence potential of Escherichia coli isolates from skin and soft tissue infections,” *J. Clin. Microbiol.*, vol. 47, no. 6, pp. 1811–1817, 2009.